ELSEVIER

Burned area mapping using multi-temporal moderate spatial resolution data—a bi-directional reflectance model-based expectation approach

D.P. Roy [a,b,*], P.E. Lewis [c], C.O. Justice [d]

[a]Department of Geography, 1113 LeFrak Hall, University of Maryland, College Park, MD 20742, USA
[b]NASA Goddard Space Flight Center, Code 922, USA
[c]Remote Sensing Unit, Department of Geography, University College London, 26 Bedford Way, London WC1H 0AP, UK
[d]Department of Geography, 1113 LeFrak Hall, University of Maryland, College Park, MD 20742, USA

Abstract

While remote sensing offers the capability for monitoring land surface changes, extracting the change information from satellite data requires effective and automated change detection techniques. The majority of change detection techniques rely on empirically derived thresholds to differentiate changes from background variations, which are often considered noise. Over large areas, reliable threshold definition is problematic due to variations in both the surface state and those imposed by the sensing system. A new approach to change detection, applicable to high-temporal frequency satellite data, that maps the location and approximate day of change occurrence is described. The algorithm may be applied to a range of change detection applications by using appropriate wavelengths. The approach is applied here to the problem of mapping burned areas using moderate spatial resolution satellite data. A bi-directional reflectance model is inverted against multi-temporal land surface reflectance observations, providing an expectation and uncertainty of subsequent observations through time. The algorithm deals with angular variations observed in multi-temporal satellite data and enables the use of a statistical measure to detect change from a previously observed state. The algorithm is applied independently to geolocated pixels over a long time series of reflectance observations. Large discrepancies between predicted and measured values are attributed to change. A temporal consistency threshold is used to differentiate between temporary changes considered as noise and persistent changes of interest. The algorithm is adaptive to the number, viewing and illumination geometry of the observations, and to the amount of noise in the data. The approach is demonstrated using 56 days of Moderate Resolution Imaging Spectroradiometer (MODIS) land surface reflectance data generated for Southern Africa during the 2000 burning season. Qualitatively, the results show high correspondence with contemporaneous MODIS active fire detection results and reveal a coherent spatio-temporal progression of burning. Validation of these results is in progress and recommendations for future research, pending the availability of independent validation data sets, are made. This approach is now being considered for the MODIS burned area algorithm.
© 2002 Elsevier Science Inc. All rights reserved.

1. Introduction

Fire occurs throughout the world with local to regional impacts on land use, productivity, carrying capacity, and biodiversity, and regional to global impacts on hydrologic, biogeochemical, and atmospheric processes. Satellite remote sensing provides the only practical means of monitoring biomass burning over large areas. The requirements for fire data articulated by the International Geosphere-Biosphere Program—Data and Information Systems (IGBP-DIS) on behalf of the scientific community to the Committee on Earth Observation Systems (CEOS) and by the Global Observation of Forest Cover (GOFC) initiative are for systems that can detect globally the timing and spatial extent of fire (GOFC Design Team, 1999; Justice, 1999). This information is required by researchers to understand the basic relationships between fire, population, and land use (Frost, 1999) and to allow managers, planners, and policy makers the opportunity to understand fires in their environmental, economic, and social contexts and to formulate their responses accordingly (Stocks, Goldammer, Cahoon, & Frost, 1999). At regional to global scales, this information is required to estimate trace gas and particulate emissions associated with natural and anthropogenic fires, important for understanding loss of

---

* Corresponding author. Department of Geography, 1113 LeFrak Hall, University of Maryland, College Park, MD 20742, USA.
E-mail address: droy@kratmos.gsfc.nasa.gov (D.P. Roy).

biomass and release of carbon and greenhouse gasses to the atmosphere (Levine, 1996).

Monitoring of biomass burning using satellite data has considerable heritage. Global active fire detection is provided using hotspot detection algorithms working on thermal channel data from the National Oceanic and Atmospheric Administration (NOAA) Advanced Along Track Scanning Radiometer (AVHRR) (Giglio, Kendall, & Justice, 1999; Stroppiana, Pinnock, & Gregoire, 2000), European Space Agency (ESA) Along Track Scanning Radiometer (ATSR) (Arino & Rosaz, 1999) and the National Aeronautics and Space Administration (NASA) Moderate Resolution Imaging Spectroradiometer (MODIS) sensors (Justice et al., 2002, this issue; Kaufman et al., 1998). The timing and spatial extent of burning cannot be estimated reliably from these orbital hot spot data, as the satellite may not overpass when burning occurs and because clouds may preclude active fire detection. Burned area mapping algorithms that examine spectral changes, rather than relying on hotspot detection, are generally insensitive to these effects as spectral changes induced by burning are temporally persistent. Burned areas are characterized by deposits of charcoal and ash, by the removal of vegetation, and by the alteration of the vegetation structure. Persistence of the charcoal and ash signal varies as a function of climate, fire regime and fuel load, while the burn scar signal duration depends on site primary productivity and vegetation recovery (Pereira, Chuvieco, Beaudoin, & Desbois, 1997). Given that fire is an agent of land cover alteration, burned area mapping algorithms that use multi-temporal moderate spatial resolution data under a change detection scheme have received considerable attention. For example, Fredericksen, Langaas, and Mbaye (1990) mapped burned areas in Senegal by analysis of time trajectories of AVHRR reflectance; Kasischke and French (1995) used the fall in Normalized Difference Vegetation Index (NDVI), which takes place after burning, to map burned areas in Alaska with AVHRR data; Eva and Lambin (1998a) labeled burned ATSR pixels in Central Africa as those whose short-wave infrared reflectance fell with a simultaneous increase in surface brightness temperature; and Barbosa, Gregoire, and Pereira (1999) made continental burned area maps in different functional vegetation strata of Africa from AVHRR data by labeling burned pixels where a vegetation index value decreased and the surface temperature increased. In these approaches, the definition of the magnitude of spectral change associated with the conversion of vegetation to burned vegetation is critical. Composited data have typically been used to reduce threshold sensitivity to bi-directional reflectance effects and residual cloud and atmospheric contamination. Thresholds have been derived empirically by examination of other remotely sensed data (Eva & Lambin, 1998a), by examination of the difference variability of the data used to map burning over a local spatial window (Fernandez, Illera, & Casanova, 1997), by examination of the fre-

quency distribution of the data used to map burning over functional vegetation strata (Barbosa, Gregoire, et al., 1999), and by comparison of the data used to map burning with contemporaneous active fire detection results (Fraser, Li, & Cihlar, 2000; Roy, Giglio, Kendal, & Justice, 1999). While these approaches provide useful change information, their accuracy is limited by a range of complicating factors relating the surface state to the remotely sensed measurement. Thus, for example, these methods fail to account for variations in the signal as a function of sun–target–sensor geometries (McDonald, Gemmell, & Lewis, 1998). Further, they fail to exploit the full range of information available in the remote sensing signal and complicate/limit our ability to combine information from different types of sensor.

This paper presents a new generic approach to change detection for high temporal frequency satellite data that maps the location and approximate day of change occurrence. The approach is described and applied to the problem of mapping burned areas using moderate spatial resolution satellite data. This application was initially prototyped using AVHRR time series (Roy & Lewis, 2000) and since the successful launch of MODIS has been implemented and further refined using MODIS data acquired over Southern Africa. Initial MODIS results, pending a more formal quantitative validation, are presented. Like any change detection methodology, the approach is sensitive to remotely sensed variations that are not associated with changes in the surface. These problems, which include inaccurate cloud detection, poor spectral calibration, and geometric misregistration, are less prevalent in MODIS data than earlier comparable sensor data such as provided by AVHRR. The MODIS geolocation accuracy is significantly higher than provided by AVHRR (Wolfe et al., 2002, this issue) and simulations varying the number of orbits and the observation geometry indicate reduced misregistration impacts on change detection capabilities when MODIS rather than AVHRR data are used (Roy, 2000). Previous change detection methods use classification or thresholding techniques that rely on building empirical relationships between the remotely sensed signal and the scene change components. The method developed here fits a model of surface reflectance against recent observations of the surface and predicts the value of a subsequent observation to provide an expectation of current reflectance measurements. It is well known that the majority of land surfaces are strongly anisotropic reflectors at optical through to thermal wavelengths (e.g., Barnsley, Allison, & Lewis, 1997). This directional dependence in reflectance as a function of the sun–target–sensor geometry is described by the Bi-directional Reflectance Distribution Function (BRDF) (units of sr^{-1}), though a more practical quantity for relating to measurements is the Bi-directional Reflectance Factor (BRF) (unitless). Directional reflectance effects can be significant in wide field of view data. For example, Leroy and Hautecoeur (1999) found vegetation index variations of the order 0.05–0.2

due to directional effects in POLarization and Directionality of the Earth's Reflectances instrument (POLDER) data over the African continent. Failure to account for such effects implies a commensurate reduction in change detection capabilities and importantly prevents exploitation of the full range of information available in wide field of view data. The use of a model that incorporates directional reflectance effects is key to the described approach and offers an advance over previous change detection methods.

A range of models of the BRDF of snow, soils and vegetation exist (Goel & Thompson, 2000; Nolin & Liang, 2000). These models have progressed in recent years from theoretical and experimental tools to operational use in the generation of satellite-derived products, including several of the MODIS Land products. One of these is the MODIS BRDF/albedo product (Schaaf et al., 2002, this issue; Wanner et al., 1997), which uses a BRDF model to combine multiple angular observations into a description complete reflectance field and related angular integrals, which are used to calculate albedo. This can be achieved rapidly and reliably using (linear) kernel-driven models of the BRDF. The heritage of the approach to the MODIS BRDF/albedo product and the change detection algorithm developed here can be traced to the work of Roujean, Leroy, and Deschamps (1992), who first developed this class of models for normalization of BRDF effects. Lucht and Lewis (2000) recently demonstrated how the concepts contained within the (linear) BRDF modeling approach can be used to predict uncertainty in the model parameters and related products for different sensor sampling scenarios. Building on this work, a BRDF model-based expectation change detection algorithm is developed. Further justification for the choice of BRDF model is given below. The directional reflectance model is inverted against multi-temporal satellite reflectance observations sensed over a given period and used to provide an expectation and uncertainty of subsequent observations. Discrepancies between subsequent observation values and the expected values, quantified by a probability term, are attributed to surface *change* or to "noisy" data (e.g., residual cloud, shadow, etc.). The temporal consistency of discrepancies found by sliding the observation period through the time series is used to identify persistent changes. This approach has several attractive properties and provides a route for the use of multiple data sources and observations of varying degrees of uncertainty within a rigorous statistical framework.

2. Southern Africa study region and MODIS data

Southern Africa is subjected to some of the most extensive biomass burning in the world (Crutzen & Andreae, 1990). Recent global analysis of vegetation fires using satellite data has shown that the largest number of detected fires was found in the African continent (Dwyer, Pinnock, Gregoire, & Pereira, 2000). Burning in Southern Africa occurs primarily in the dry season from approximately May to November, with perturbations in the timing and burning severity controlled by anthropogenic and meteorological factors that affect the available fuel load and moisture content. This burning produces quantities of trace gasses and smoke aerosols that remain suspended in the atmosphere for long periods during the dry season (Garstang et al., 1996). In the context of the Intergovernmental Panel on Climate Change, scientists are studying the quantities of biomass burned, trace gas and aerosol emissions for Southern Africa (Braatz et al., 1995). Most of the uncertainty in emissions calculations lies in estimates of area burned and fuel loads. For example, there is a 10-fold difference in the estimated amount of biomass burned annually for Southern Africa between the work of Hao, Lui, and Crutzen (1990) and Scholes, Ward, and Justice (1996). Fires in Southern Africa occur due to natural and anthropogenic causes, primarily lightening and land management. Recent studies suggest that people have exercised significant control over fire regimes in Southern Africa since at least the Holocene (Bird & Cali, 1998).

The MODIS daily 500-m land surface reflectance product (Vermote, El Saleous, & Justice, 2002, this issue) and daily 1-km active fire product (Justice et al., 2002, this issue) are used to apply and verify the algorithm, respectively. Fig. 1 illustrates the spatial extent of the study region that lies between 10°S and 30°S, and encompasses most of Angola, Zambia, Malawi, Mozambique, all of Namibia, Botswana, Zimbabwe, and parts of South Africa and the Democratic Republic of Congo. The MODIS land surface reflectance 0.645, 0.555, and 0.469 μm bands are displayed in Fig. 1 as red, green, and blue, respectively, to give a quasi-true color representation. The illustrated data were selected by maximum NDVI compositing daily MODIS land surface reflectance data sensed from August 28 to September 28, 2000. The faint near-vertical discontinuities are caused by directional reflectance effects and occur across the region in alignment with the MODIS orbital geometry. The active fires detected over the same period are shown for illustrative purposes. In total 56 days of MODIS data acquired toward the end of the burning season, from August 20th to October 14th 2000, were used in this study. It should be noted that during this time, the MODIS instrument calibration and the MODIS land products were still being refined (Roy et al., 2002, this issue). The active fire detection algorithm was known to be under-performing, in particular it was failing to detect certain fires (Justice et al., 2002, this issue), and the cloud mask algorithm (Ackerman et al., 1998) was known to be falsely labeling certain fires and desert regions as cloud (Justice et al., 2002, this issue). Also, the land surface reflectance data were not comprehensively corrected for aerosol contamination in this period. Persistent smoke aerosols are apparent in the North of Fig. 1. All the MODIS land products used in this study were masked using the product per pixel quality assessment bits (Roy et al., 2002, this issue) to remove cloudy, bad quality, non-land, inland water, and ephemeral water pixels.
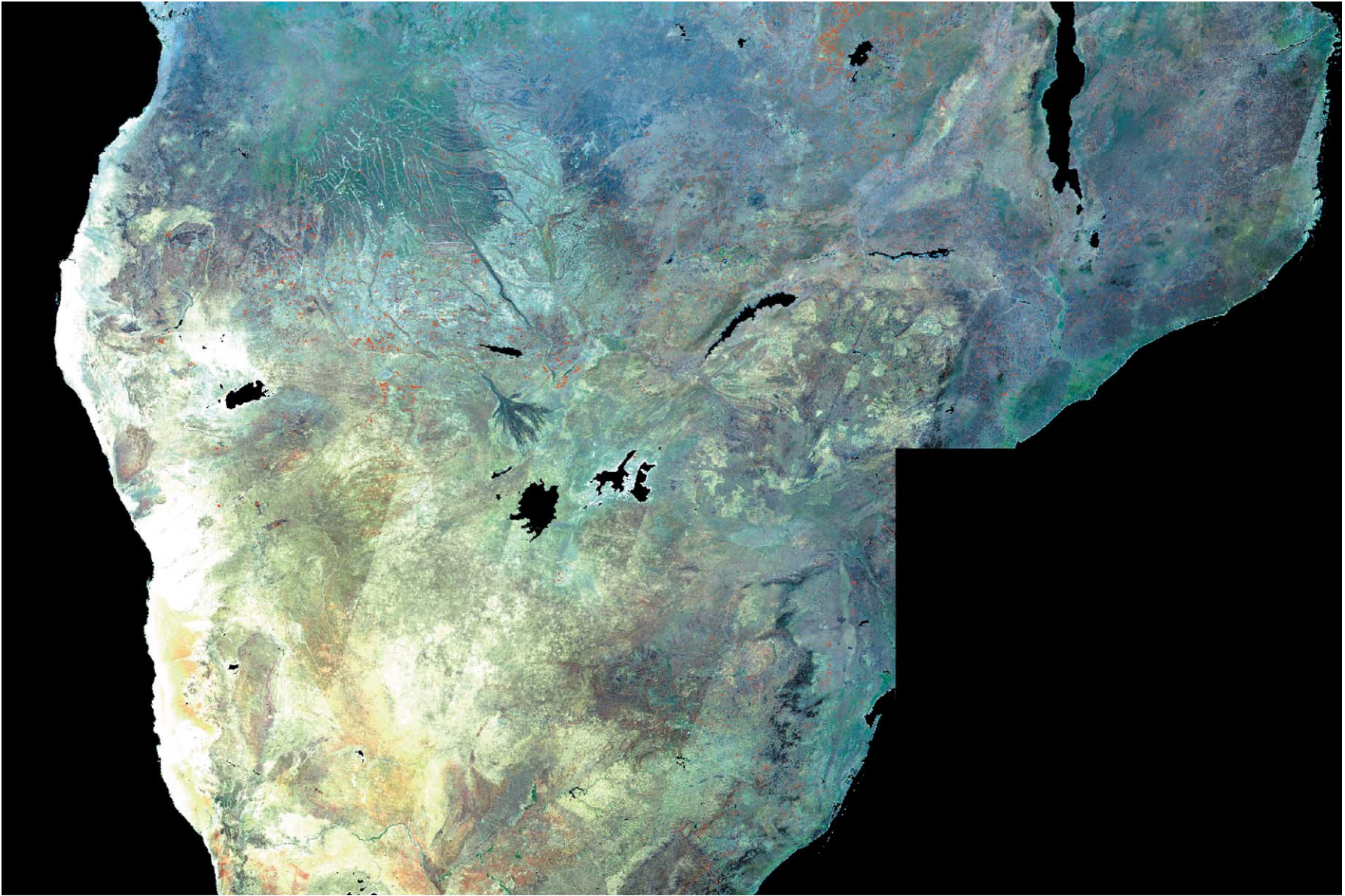
Fig. 1. Southern Africa study area. Monthly maximum NDVI composite computed from daily 500-m MODIS land surface reflectance data sensed August 28 to September 28, 2000. True color image—the composited MODIS 0.645, 0.555, and 0.469 μm reflectances are displayed as red, green, and blue, respectively. The red dots illustrate the 1-km locations of MODIS active fires detected over this month. The faint near-vertical discontinuities are caused by directional reflectance effects.

The Etosha Pan, Namibia, and the Makgadikgadi Pan, Botswana, and several other regions were consistently flagged as cloudy or ephemeral water and so appear black in Fig. 1.

3. MODIS wavelength selection

For a given change detection scheme, it is desirable to use wavelengths that are sensitive to the changes of interest while remaining insensitive to other types of change. In general, near-infrared and middle-infrared wavelengths have been found to provide stronger burned area discrimination than visible wavelengths (Pereira et al., 1997). Remotely sensed temperature estimates and thermal wavelengths have also been used to aid differentiation between burned and unburned vegetation (e.g., Cahoon, Stocks, Levine, Cofer, & Pierson, 1994; Eva & Lambin, 1998a). The spectral signature of burned areas may vary as a function of surface property variations, including the vegetation characteristics, structure, and soil background, and may also vary as a consequence of the fire behavior. Fire behavior controls the severity of fire effects including the degree and parts of the vegetation structure that are burned (ground cover, canopy cover, woody components, etc.), the patchiness of unburned vegetation, the amount of charcoal and ash deposition, and the size and spatial distribution of the burn. Post-fire revegetation and charcoal and ash dissipation by the elements may complicate the spectral signature of burned areas (Langaas, 1995).

The ability of the MODIS land surface reflectance bands to discriminate between burned and unburned vegetation is quantified and used to identify appropriate wavebands for application to burned area mapping in the study region. MODIS has seven reflective bands for land studies, from the visible to middle infrared wavelengths. The seven bands are centered on wavelengths 0.645, 0.858, 0.469, 0.555, 1.240, 1.640, and 2.130 μm (bands 1–7, respectively) with variable bandwidths between 20 and 50 nm (Barnes, Pagano, & Salomonson, 1998). The reflective component of the middle infrared shows potential for burned–unburned discrimination but is not considered in this paper as this MODIS product is still experimental (Petitcolin & Vermote, 2002, this issue). The ability of the seven MODIS land surface reflectance bands to discriminate between burned and unburned vegetation is quantified by examination of these data at locations where MODIS active fires were detected. Only locations where at least three non-cloudy, good quality observations were sensed in the 4 days occurring before the active fire detection and at least three non-cloudy good quality observations were sensed in the 4 days occurring after the fire detection are considered. The values observed in the 4 days occurring before and after the active fire detection are labeled as unburned and burned, respectively. Observations sensed with a view zenith greater than 45° are not used, as the surface area sensed by the MODIS instanta-

neous field of view increases rapidly above this zenith angle (Wolfe, Roy, & Vermote, 1998). A month of MODIS data for the region illustrated in Fig. 1 are considered, giving a total of more than 15,000 burned and 15,000 unburned values for each MODIS band. Fig. 2 shows mean ± 1 standard deviation summary statistics of the burned (filled circles) and unburned (open circles) values for the different bands. For all bands, burning reduces the mean land surface reflectance, although for bands 1, 3, 4, and 7, the difference between the mean unburned and burned reflectance values is small compared to the standard deviations of these data. Fig. 3 shows the burned–unburned separability of these data computed using the Bhattacharyya distance measure (Fukunaga, 1990). The separability of the NDVI, derived from MODIS bands 1 and 2, and the daily MODIS land surface temperature product (Wan, Zhang, Zhang, & Li, 2002, this issue) are also shown. The Bhattacharyya distance is bounded between values of 0 (low separability) and 2 (high separability), and is monotonically related to classification accuracy when probability distribution class models (e.g., maximum likelihood) are used. The separability of these data are fairly low due to factors that may include active fire detection commission errors, residual cloud contamination, reduced variance found in off-nadir observations, and directional reflectance effects. The results shown in Figs. 2 and 3 indicate that for the Southern Africa study area MODIS band 5 (1.240 μm) land surface reflectance provides the highest burned–unburned discrimination followed by band 2 (0.858 μm) and band 6 (1.640 μm). The MODIS band 1 (0.645 μm), NDVI, and land surface temperature data provide relatively poor discrimination, and bands 3 (0.469 μm), 4 (0.555 μm), and 7 (2.130 μm) provide almost no discrimination. The low discrimination provided by the shorter wavelength bands 3, 4, and 1 is in part due to their sensitivity to scattering by smoke aerosols (Kaufman & Remer, 1994; Miura, Huete, van Leeuwen, & Didan, 1998).

Fig. 4 illustrates MODIS bands 6, 5, and 2 data sensed on three separate days over a region of active burning near the Angolan–Nambian border. The region is primarily open woodland (*teak*, *kiaat*, *false mopane*, *combretum*, and *terminalia* tree species) on deep Kalahari sand, with some grassy areas occurring in dune streets (J. Le Roux, Etosha Ecological Institute, Nambia, personal communication). Fig. 4A shows the region sensed on Julian day 246 (September 2nd 2000), and Fig. 4B and C shows the same region 20 and 40 days later. The progression of several extensive burns are clearly evident in these wavebands. The Okavango River marks the border and runs East–West across the illustrated 200 × 250 km region. The border town of Rundu and its service roads have high reflectance values (light tones), and the extensive burned areas to south and north of the border have low reflectance (dark tones). The more recent burns generally have lower bands 6, 5, and 2 reflectance and so appear darker than the older burns. No smoke is evident in these data because MODIS bands 6, 5, and 2 are largely
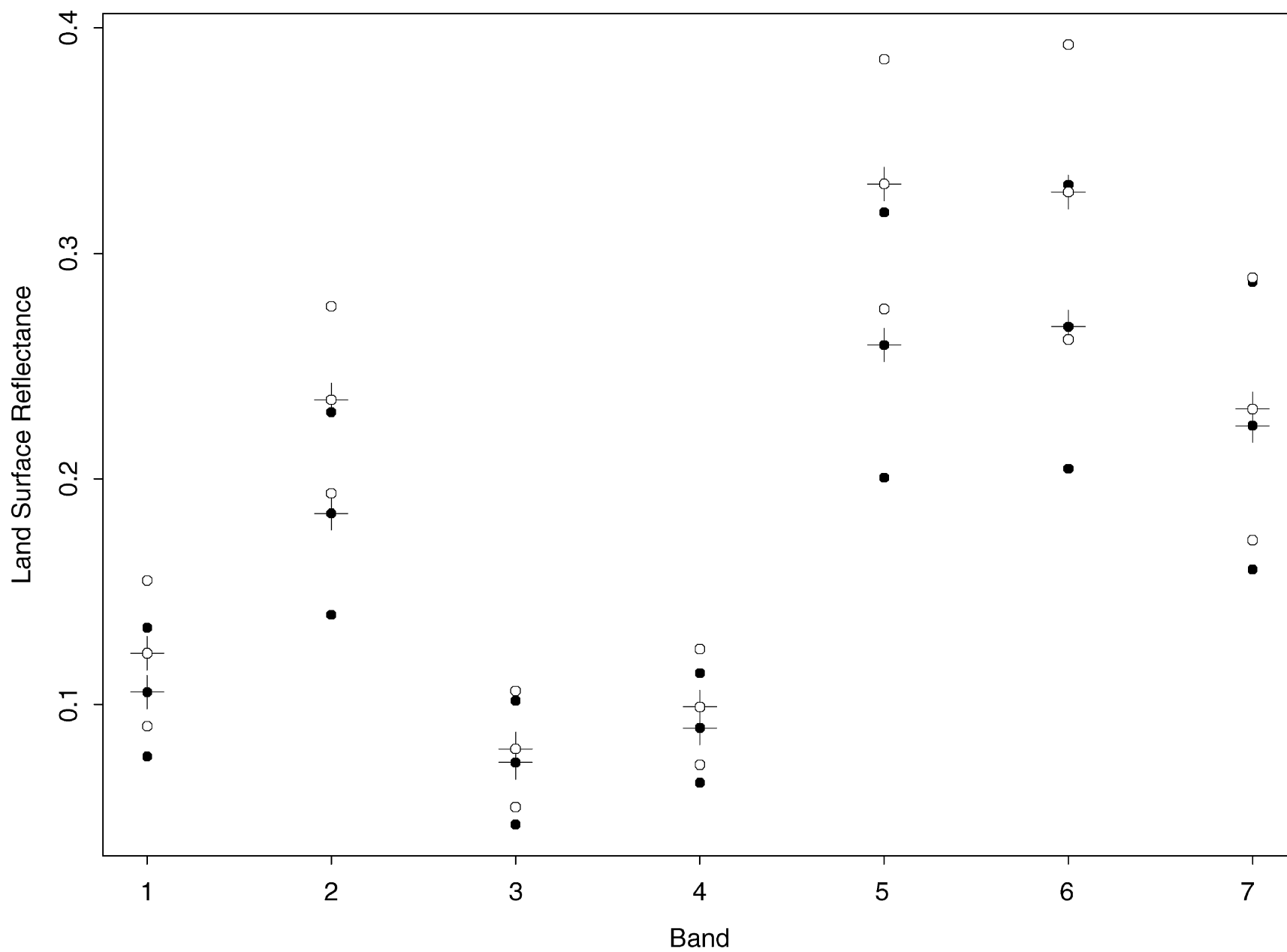
Fig. 2. Unburned (open circles) and burned (filled circles) land surface reflectance summary statistics for the seven MODIS reflective bands. Mean reflectance (circle superimposed on cross) and mean ± 1 standard deviation reflectance (circles without crosses) values are shown. These data computed from more than 15,000 burned and 15,000 unburned values over a month of data from the region illustrated in Fig. 1.
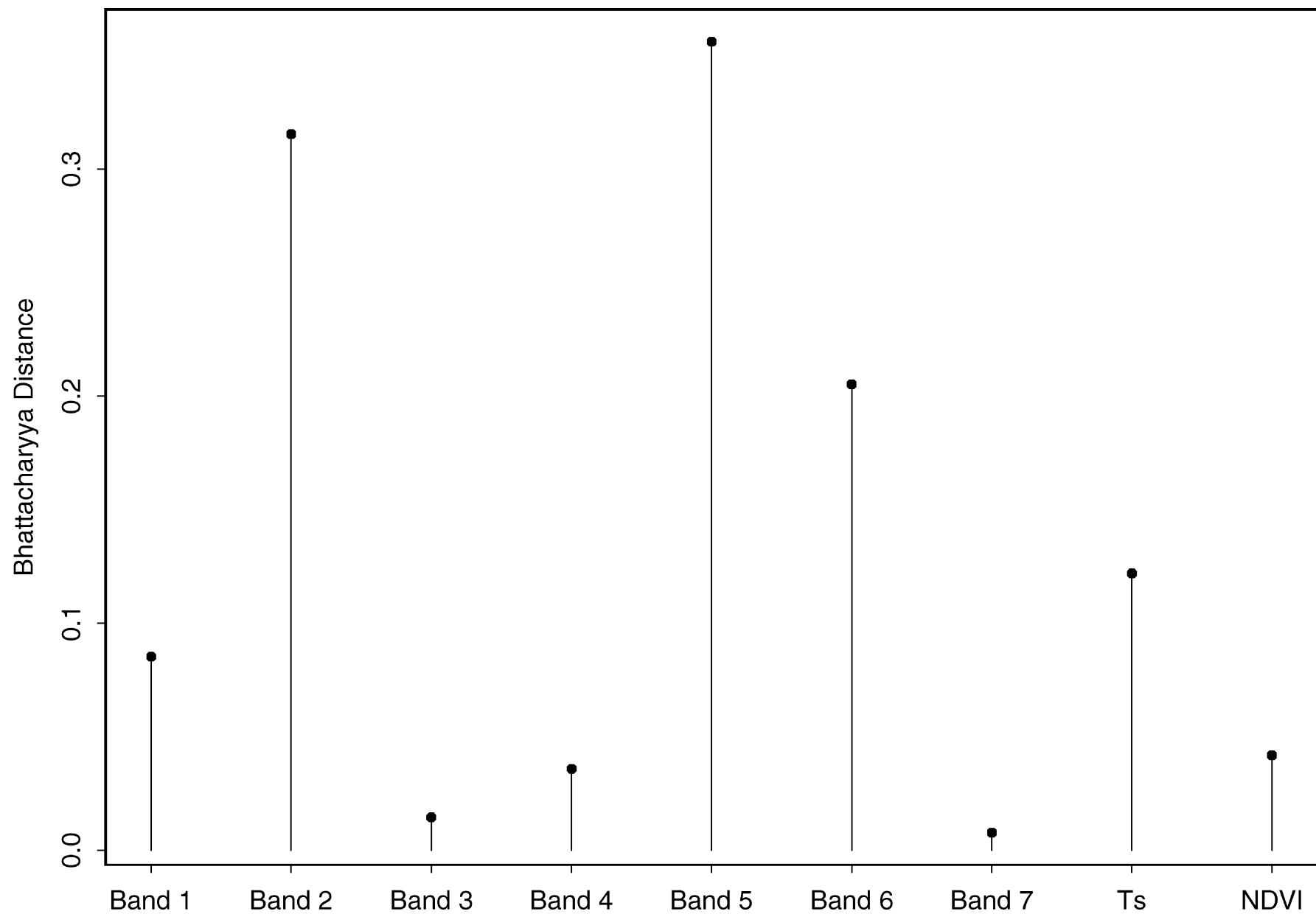
Fig. 3. Burned−unburned separability of the seven MODIS land surface reflectance bands, NDVI, and the MODIS land surface temperature (Ts) product. These data computed from more than 15,000 burned and 15,000 unburned values over a month of data from the region illustrated in Fig. 1.
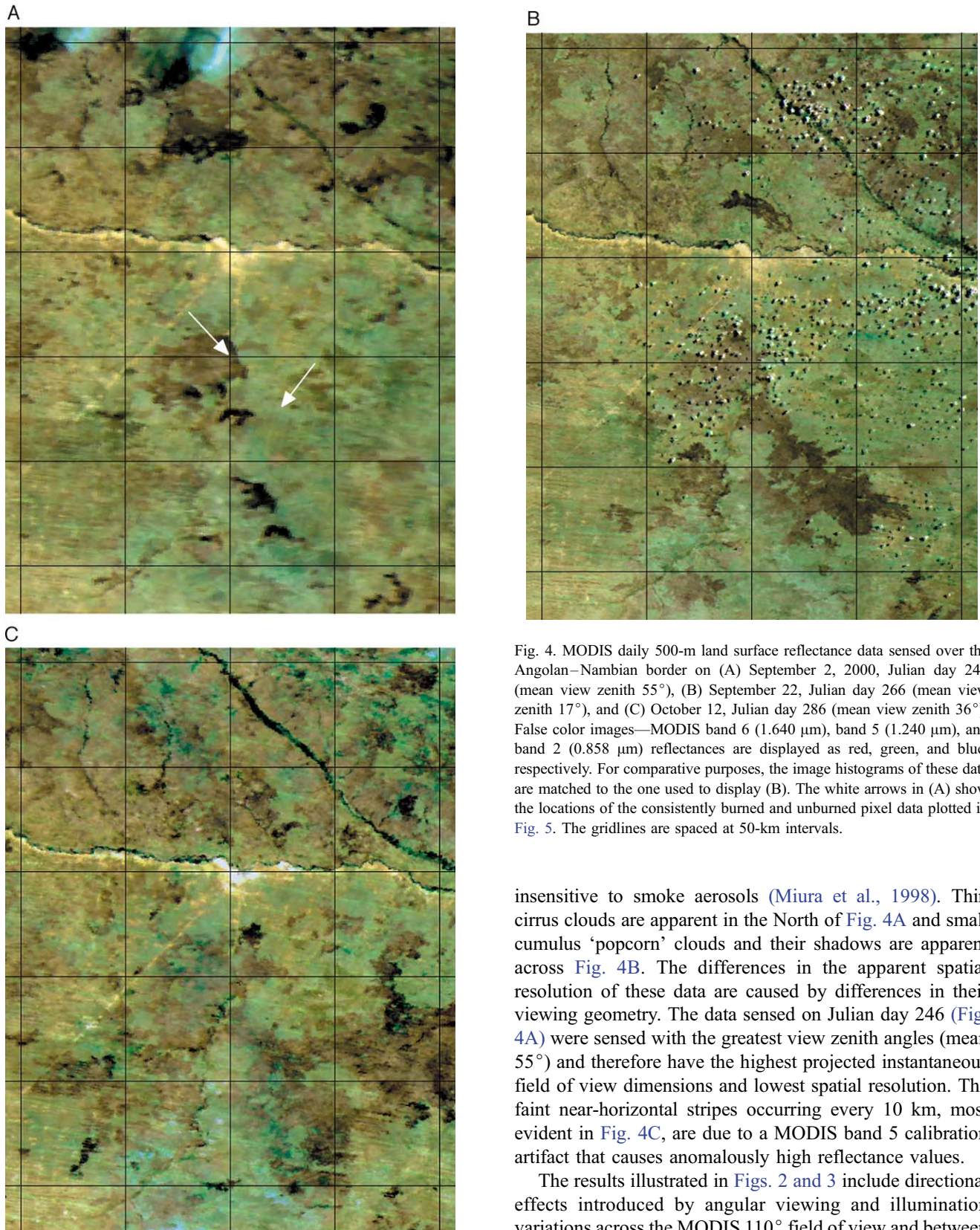
A

B

C

Fig. 4. MODIS daily 500-m land surface reflectance data sensed over the Angolan–Nambian border on (A) September 2, 2000, Julian day 246 (mean view zenith 55°), (B) September 22, Julian day 266 (mean view zenith 17°), and (C) October 12, Julian day 286 (mean view zenith 36°). False color images—MODIS band 6 (1.640 μm), band 5 (1.240 μm), and band 2 (0.858 μm) reflectances are displayed as red, green, and blue, respectively. For comparative purposes, the image histograms of these data are matched to the one used to display (B). The white arrows in (A) show the locations of the consistently burned and unburned pixel data plotted in Fig. 5. The gridlines are spaced at 50-km intervals.

insensitive to smoke aerosols (Miura et al., 1998). Thin cirrus clouds are apparent in the North of Fig. 4A and small cumulus 'popcorn' clouds and their shadows are apparent across Fig. 4B. The differences in the apparent spatial resolution of these data are caused by differences in their viewing geometry. The data sensed on Julian day 246 (Fig. 4A) were sensed with the greatest view zenith angles (mean 55°) and therefore have the highest projected instantaneous field of view dimensions and lowest spatial resolution. The faint near-horizontal stripes occurring every 10 km, most evident in Fig. 4C, are due to a MODIS band 5 calibration artifact that causes anomalously high reflectance values.

The results illustrated in Figs. 2 and 3 include directional effects introduced by angular viewing and illumination variations across the MODIS 110° field of view and between
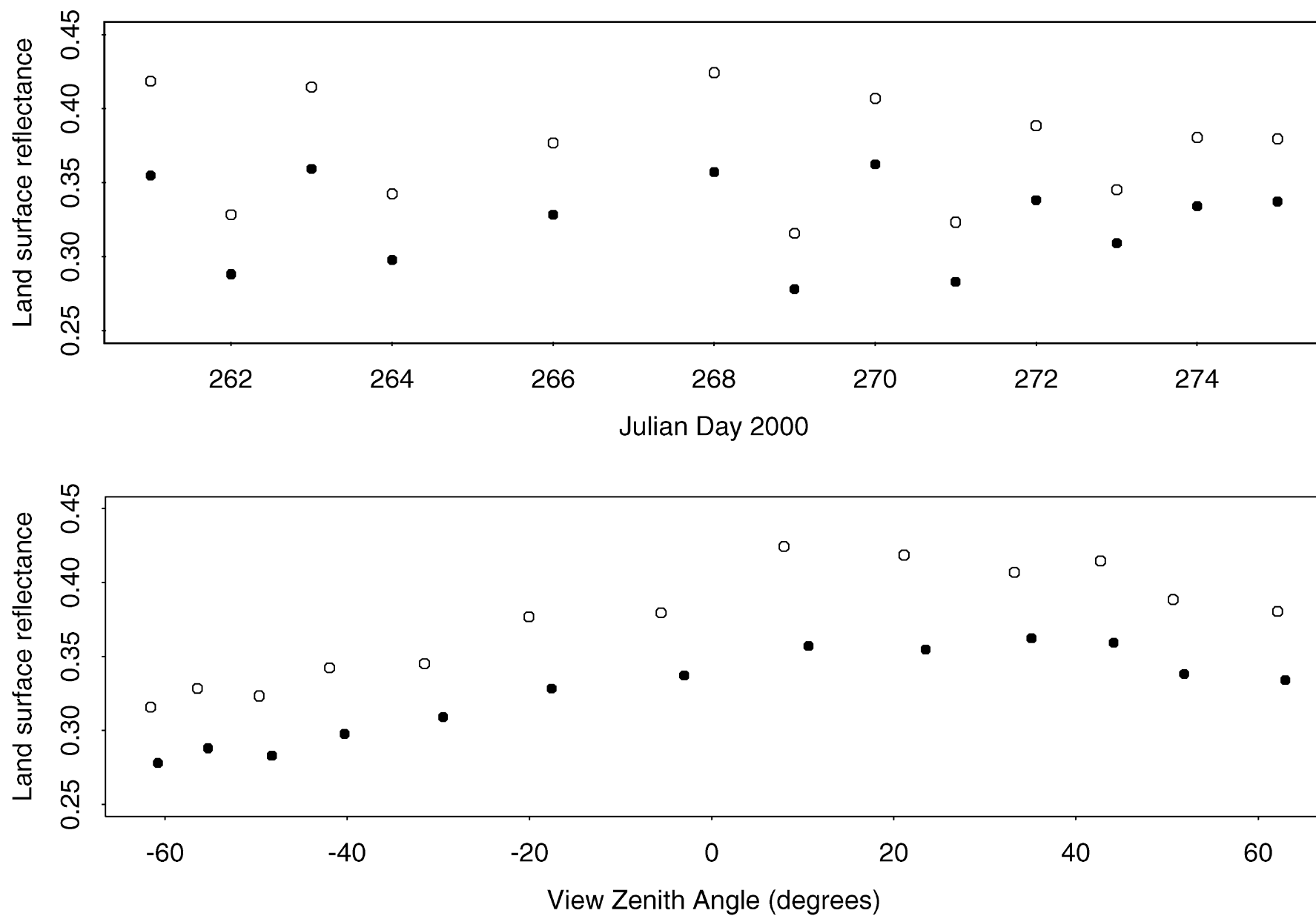
Fig. 5. MODIS band 5 (1.240 μm) land surface reflectance values for consistently burned (filled circles) and unburned (open circles) pixels sensed over a 16-day period from September 16 (Julian day 260) to October 1, 2000 (Julian day 275). These data sensed with off-principal plane azimuthal sampling and a 26° mean solar zenith angle. Arrows shown in Fig. 4A mark the burned and unburned pixel locations.

consecutive MODIS orbits over the 16-day MODIS repeat cycle (Wolfe et al., 2002, this issue). These directional effects are illustrated in Fig. 5, which shows daily band 5 land surface reflectance values for two pixels that were unburned (open circles) and burned (filled circles) over a 16-day period. These data were extracted at the locations illustrated in Fig. 4A and were sensed with off-principal plane azimuth angles and a 26° mean solar zenith angle. The temporal reflectance variability is seen to be primarily due to directional effects when the data are plotted as a function of view zenith angle rather than time. The directional reflectance plotted in the lower panel of Fig. 5 also include effects due to variations in the solar zenith angle (from 22° to 33°) and the relative azimuth (29° variation) of the observations. However, the variation in view zenith angle is much greater than either of these two. The 'shape' of the directional reflectance as a function of view zenith angle is typical of that expected for open woodland with off-principal plane azimuthal sampling (Ni & Jupp, 2000). It shows a broad peak in the retro-reflection direction due to shadow hiding, and a steady decrease in the forward-scattering direction (negative view zenith angles) due to increased proportions of shadowed crowns and ground being viewed. The difference between the maximum unburned near-nadir and far-off nadir reflectance values is more than 0.10. This difference is greater than the difference between the burned and unburned daily reflectance values and implies that burned–unburned reflectance thresholds that do not take directional reflectance effects into account may work ineffectively.

4. Generic change algorithm

Fig. 5 suggests that a large proportion of the variation in observed reflectance might be attributed to directional effects. These angular variations may be modeled by inverting a BRDF model against satellite observations of reflectance. It follows that, under the assumption that the surface conditions do not change, the inverted BRDF model parameters may be used to predict satellite observations at other viewing and illumination angles. Any large discrepancies between predicted and measured values may then be attributed to surface *change* or "bad" data (residual cloud, shadow, etc.).

We chose to make use of the BRDF modeling approach of Roujean et al. (1992) in this application. The approach has been extended by Wanner, Li, and Strahler (1995) and is implemented in the MODIS BRDF/albedo product (Schaaf et al., 2002, this issue; Wanner et al., 1997). It considers the BRF as a linear combination of kernels (functions of viewing and illumination angles only), which account for the scattering properties of a wide variety of land surface materials (Schaaf et al., 2002, this issue). The kernels are derived from abstractions of physically based modeling considerations. Generally, three kernels are used, quantify-

ing the angular behavior of "volumetric" scattering from a homogeneous medium (based on radiative transfer theory), shadowing/obstruction effects of surface protrusions (based on geometric optics theory), and an isotropic term to account for multiple-scattering and to act as an angular normalization term (reflectance at nadir with nadir illumination). The ambrals model in the MODIS BRDF/albedo product, and the work presented here use kernels known as RossThick (an optically thick approximation to volumetric scattering) and LiSparseReciprocal (an approximation to protrusion effects for sparsely populated surfaces modified for conditions of reciprocity). The particular kernel set used, and indeed the wider choice of BRDF model type, is unlikely to affect an algorithm such as that considered here. We are not directly interested in the model parameters but only in the ability of the model to mimic observed reflectances and predict reflectance at similar viewing and illumination angles. The MODIS angular sampling is primarily a view zenith angle variation close to a single azimuthal plane, and consequently, the requirements of the model are less stringent than on one required to predict over all angles. We consider the details of model selection a topic for further research, but note that the kernel-driven approach meets the requirements for this application. In particular, the following can be noted for kernel-driven models (Lucht & Roujean, 2000): (i) inversion of a linear model is achieved analytically (hence rapidly) and has a single (unconstrained) solution; (ii) assuming linear scaling of reflectance fields leads to implicit modeling of heterogeneity; (iii) linear modeling allows rapid prediction of uncertainty in the model parameters and linear combinations thereof (Lucht & Lewis, 2000).

Following this approach then, and denoting the volumetric kernel $k_{\mathrm{vol}}(\Omega,\Omega')$ and the protrusion kernel $k_{\mathrm{GO}}(\Omega,\Omega')$, the spectral BRF at wavelength λ, $\rho(\lambda,\Omega,\Omega')$ is given by:

$$\rho(\lambda, \Omega, \Omega') = \underline{P} \cdot \underline{K} \qquad (1)$$

where Ω represents the viewing vector, Ω' the illumination vector, and:

$$\underline{K} = [\,1 \quad k_{\mathrm{vol}}(\Omega,\Omega') \quad k_{\mathrm{GO}}(\Omega,\Omega')\,]^{\mathrm{T}}$$

$$\underline{P} = [\,f_{\mathrm{iso}} \quad f_{\mathrm{vol}} \quad f_{\mathrm{GO}}\,]^{\mathrm{T}}$$

$\underline{P}$ is the parameter vector, $\underline{K}$ a vector containing the kernel values, and $^{\mathrm{T}}$ denotes the transpose operation. f_{iso}, f_{vol}, and f_{GO} are the model parameters for the isotropic, volumetric scattering, and protrusion kernels, respectively. Being a linear model, Eq. (1) can be inverted analytically against a set of m observations of spectral BRF, $\rho_{\mathrm{obs}}(\lambda,\Omega_i,\Omega_i')$ using the method of least squares (Whittaker & Robinson, 1960). This can be stated as:

$$\underline{M}\,\underline{P} = \underline{V} \qquad (2)$$

where $\underline{\underline{M}}$ is a symmetric matrix:

$$\underline{\underline{M}} = \sum_{i=1}^{i=m} \begin{bmatrix} 1 & k_{\text{vol}}(\Omega_i, \Omega_i') & k_{\text{GO}}(\Omega_i, \Omega_i') \\ \cdots & k_{\text{vol}}(\Omega_i, \Omega_i')^2 & k_{\text{vol}}(\Omega_i, \Omega_i')k_{\text{GO}}(\Omega_i, \Omega_i') \\ \cdots & \cdots & k_{\text{GO}}(\Omega_i, \Omega_i')^2 \end{bmatrix}$$

$$\underline{V} = \sum_{i=1}^{i=m} [\rho(\lambda, \Omega_i, \Omega_i') \quad \rho(\lambda, \Omega_i, \Omega_i')k_{\text{vol}}(\Omega_i, \Omega_i')$$
$$\rho(\lambda, \Omega_i, \Omega_i')k_{\text{GO}}(\Omega_i, \Omega_i')]^T$$

The solution to the model parameters is found by multiplying both sides of Eq. (2) by the inverse of matrix $\underline{\underline{M}}$, $\underline{\underline{M}}^{-1}$, in the standard way. Additionally, we can note that for a linear model of this sort (Lucht & Lewis, 2000; Whittaker & Robinson, 1960), the mean error in a prediction of BRF ("standard error of the estimate"), ε, is given by:

$$\varepsilon = e\sqrt{\frac{1}{w}} \tag{3}$$

where e is the expectation of error in an observation (assumed equal for all observations for the present), and w is the 'weight of determination' of the BRF, given by:

$$\frac{1}{w} = \underline{K}^T \underline{\underline{M}}^{-1} \underline{K}$$

e can be approximated from the residuals:

$$e^2 = \frac{1}{m-3} \sum_{i=1}^{i=m} (\rho(\lambda, \Omega_i, \Omega_i') - \rho_{\text{obs}}(\lambda, \Omega_i, \Omega_i'))^2 \tag{4}$$

Using standard statistical methods, and assuming a normal distribution of residuals, we can define a Z-score, Z, as a normalized measure related to the probability of a new candidate observation of BRF belonging to the same set as that used in the model inversion:

$$Z = \frac{\rho_{\text{cand}}(\lambda, \Omega, \Omega') - \rho(\lambda, \Omega, \Omega')}{\varepsilon} \tag{5}$$

where $\rho(\lambda, \Omega, \Omega')$ is the model predicted BRF, ε is the model prediction error, and $\rho_{\text{cand}}(\lambda, \Omega, \Omega')$ is a new candidate observation of BRF.

Thus, the generic change detection algorithm is to invert a BRF model against m BRF observations (Eq. (2)) and use the resulting model parameters to compute a predicted BRF (Eq. (1)) and Z-score (Eq. (5)) for the viewing and illumination angles of a new subsequent observation. The magnitude of the Z-score is related to the probability of the new observation *not* having the same BRF as the m observations. The sign of the Z-score is related to the increase or decrease of the new observation BRF relative to the predicted BRF. Candidate change observations are those where $|Z| \geq Z_{\text{threshold}}$ and where the sign of the Z-score indicates a BRF change in the required direction. It is clearly preferable to threshold a statistical measure of this sort rather than threshold reflectance or vegetation indices. If a change is not detected by this algorithm, it is because there was insufficient evidence provided by the observations. The method is adaptive to the viewing and illumination angles of the new observation, as well as the angular distribution and number (m) of the previous samples used in the modeling. It is also adaptive to the amount of noise in the data, through Eq. (4).

As part of the generic algorithm, we can consider two main types of 'change': temporary and persistent. The former might include short-lived effects due to soil moisture changes, shadows, undetected residual clouds, and data artifacts. These change types may be separated by examining the temporal consistency of Z-score values built by applying the algorithm in fixed temporal increments through a time series of BRF observations. Persistent changes are defined to be those for which subsequent observations over the next N_{duration} period are labeled as change candidates (i.e., $|Z| \geq Z_{\text{threshold}}$) and that have the same sign Z-score. Any other change candidates are taken to be temporary. In the current implementation, we consider a persistent change as one that has a minimum number of N_{pass} observations within the N_{duration} time period labeled as change candidates. A suitable N_{duration} value may be derived empirically for a given $Z_{\text{threshold}}$ or may be based on field observations or spectral measurements of burn persistence (e.g., Trigg & Flasse, 2000). A suitable N_{pass} value may be estimated from understanding of the satellite overpass frequency and the likely frequency of missing observations due to cloud cover, etc. The final persistent change candidate, used to estimate the day of the change, is selected as the one with the greatest $|Z|$.

Having detected a persistent change, the next task is to determine the nature of the change. (Figs. 2, 4 and 5) demonstrate that the impact of burning is to reduce the reflectance at all view angles in sensitive wavebands. To express such a consideration in a consistent framework, we examine both the magnitude and the sign difference between a modeled nadir-viewing BRF (at mean solar zenith angle) computed before and after the date of the detected persistent change to differentiate between different types of change. This follows the concept that land cover changes, such as deforestation, flooding, or burning, have different trajectories in spectral space (Zhan et al., 2002, this issue). It is also likely that different agents of change will lead to varying behavior in the directional domain, i.e., that a comparison of the BRDF model parameters before and after the change event would provide information on the agent of change. We do not, however, currently have sufficient data on this to consider its implementation.

5. MODIS algorithm implementation

The generic change algorithm is applied to MODIS band 5 (1.240 μm) 500-m land surface reflectance data as they

provide the highest burned–unburned separability (Figs. 2 and 3) and are largely insensitive to smoke aerosols. MODIS senses a single angular sample of the BRF of a particular location on each overpass of the Terra satellite. Except near the pole, the surface is viewed from a different direction by consecutive MODIS overpasses over its 16-day repeat cycle. Consequently, co-registered overlapping MODIS data sensed over a short time window must be used to build up a set of m observations required to invert the RossThick–LiSparseReciprocal BRDF model. In this application, and in line with the periods chosen for the MODIS BRDF/albedo product (Schaaf et al., 2002, this issue), we use a 16-day time window and require m to be at least seven. In this way, the BRDF model is inverted against at least seven MODIS observations sensed over a 16-day period and the Z-score is calculated to test for change on the following day. Where there are less than seven observations, for example, due to cloud cover, no inversion is performed. The 16-day window is moved in daily increments in order to detect change through a multi-temporal data set and to differentiate persistent changes from temporary changes. The algorithm is applied independently for each geolocated pixel defined within the MODIS land product tile grid (Wolfe et al., 1998).

After a persistent change candidate is identified the magnitude and the sign difference between the nadir BRF modeled reflectance computed for a mean solar zenith angle from 16 days of MODIS observations sensed before the change date, $\bar{\rho}_{\text{nadir}}^{-}$ (1.24 μm), and after the change date, $\bar{\rho}_{\text{nadir}}^{+}$ (1.24 μm), are used in an attempt to identify changes that are not due to burning. We consider the relative change in nadir BRF modeled reflectance defined as:

$$\delta\bar{\rho}_{\text{nadir}} = \frac{\bar{\rho}_{\text{nadir}}^{+}\ (1.24\ \mu m) - \bar{\rho}_{\text{nadir}}^{-}\ (1.24\ \mu m)}{\bar{\rho}_{\text{nadir}}^{-}\ (1.24\ \mu m)} \quad (6)$$

In this way, a decrease in reflectance caused by burning gives a negative $\delta\bar{\rho}_{\text{nadir}}$, and an increase in reflectance (e.g., cloud contamination) gives a positive $\delta\bar{\rho}_{\text{nadir}}$. Changes where $\delta\bar{\rho}_{\text{nadir}}$ are greater than a specified threshold are discarded as not being associated with burning. This difference is not calculated where there are less than seven observations available in the 16-day periods before and after the change candidate date. Reflectance thresholds based on relative rather than absolute changes are used to account for variability of background spectral values due to biome type, soil characteristics, etc. (Eva & Lambin, 1998a), and may possibly allow sub-pixel change detection. The size and spatial distribution of the burned area and the spectral contrast between the burned area and the surrounding cover types may bias the effectiveness of such thresholds (Eva & Lambin, 1998b) as will the sensor's radiometric and geometric characteristics. The impact of uncertainty in the modeled nadir reflectances needs further consideration, however, as does the impact of realistic models for nadir reflectance under different burn scenarios. Again, we have insufficient information to investigate this at the time of writing.

An additional heuristic found to be useful in determining the nature of change was to only consider a pixel as burned when:

$$\bar{\rho}_{\text{nadir}}^{-}\ (1.24\ \mu m) - \bar{\rho}_{\text{nadir}}^{-}\ (2.13\ \mu m)$$
$$> \bar{\rho}_{\text{nadir}}^{+}\ (1.24\ \mu m) - \bar{\rho}_{\text{nadir}}^{+}\ (2.13\ \mu m) \quad (7)$$

The justification for Eq. (7) is that burning causes a reduction in the band 5 (1.240 μm) reflectance but very little change in band 7 (2.130 μm) reflectance (Figs. 2 and 3), whereas persistent cloud, shadow, or soil moisture changes would have a similar effect in both bands. Note that both bands 5 and 7 are insensitive to smoke aerosols (Miura et al., 1998). Considering the difference between reflectance in these two wavebands therefore compensates for overall brightness variations across the scene and distinguishes burns from factors that have the same effect across both bands. It is recognized that thresholding using Eqs. (6) and (7) may not remove all non-biomass burning changes. However, at the time of writing, insufficient study of commission errors has been undertaken. Further research is required, pending the availability of independent validation data.

6. Illustrative results

Fig. 6 illustrates the results of a single step of the 16-day sliding window applied to a time series of MODIS band 5 reflectance data for the region shown in Fig. 4. Fig. 6A shows the observed MODIS land surface reflectance on day 275. The predicted reflectances computed by applying BRDF model parameters computed from days 259–274 to the day 275 solar and viewing geometry are shown in Fig. 6B. The predicted reflectances are similar to the observed day 275 reflectances except where changes have occurred. The day 275 band 5 calibration stripe artifacts have positive Z-score values, shown in Fig. 6C. The substantial burns that occurred up to and on day 275 have large negative Z-score values. The greatest Z-score magnitudes generally occur along the burn edges where changes in reflectance occurred most recently.

Fig. 7A and B illustrates results found by applying the 16-day sliding window 2 days later to the time series used to produce the results shown in Fig. 6. The progression of the burning over the 2-day period is seen by comparing the reflectances sensed on days 275 and 277 (Figs. 6A and 7A), and the Z-score data for these 2 days (Figs. 6C and 7C). There is more apparent noise in Fig. 7C than Fig. 6C, which is associated with smaller model prediction errors for day 277 and the band 5 calibration stripe artifacts. Comparison of the predicted reflectance values, Figs. 6B and 7B, indicate that they are not markedly reduced in regions that only recently burned. This is because in these regions the preceding 16 days of data were mainly unburned and so the BRDF model inversion is performed against predom-
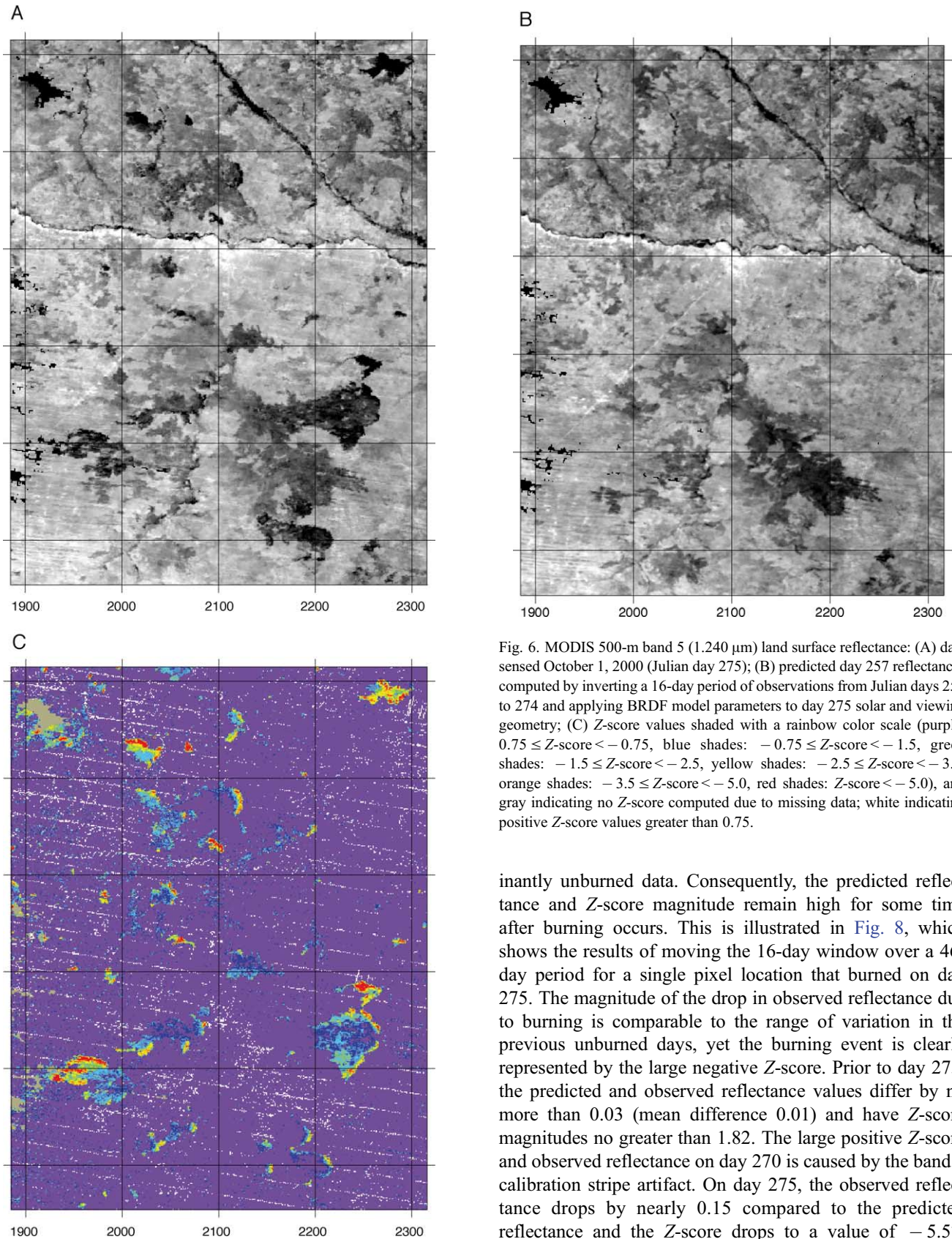
A

B

C

Fig. 6. MODIS 500-m band 5 (1.240 μm) land surface reflectance: (A) data sensed October 1, 2000 (Julian day 275); (B) predicted day 257 reflectances computed by inverting a 16-day period of observations from Julian days 259 to 274 and applying BRDF model parameters to day 275 solar and viewing geometry; (C) Z-score values shaded with a rainbow color scale (purple: $0.75 \leq Z\text{-score} < -0.75$, blue shades: $-0.75 \leq Z\text{-score} < -1.5$, green shades: $-1.5 \leq Z\text{-score} < -2.5$, yellow shades: $-2.5 \leq Z\text{-score} < -3.5$, orange shades: $-3.5 \leq Z\text{-score} < -5.0$, red shades: $Z\text{-score} < -5.0$), and gray indicating no Z-score computed due to missing data; white indicating positive Z-score values greater than 0.75.

inantly unburned data. Consequently, the predicted reflectance and Z-score magnitude remain high for some time after burning occurs. This is illustrated in Fig. 8, which shows the results of moving the 16-day window over a 46-day period for a single pixel location that burned on day 275. The magnitude of the drop in observed reflectance due to burning is comparable to the range of variation in the previous unburned days, yet the burning event is clearly represented by the large negative Z-score. Prior to day 275, the predicted and observed reflectance values differ by no more than 0.03 (mean difference 0.01) and have Z-score magnitudes no greater than 1.82. The large positive Z-score and observed reflectance on day 270 is caused by the band 5 calibration stripe artifact. On day 275, the observed reflectance drops by nearly 0.15 compared to the predicted reflectance and the Z-score drops to a value of -5.57.
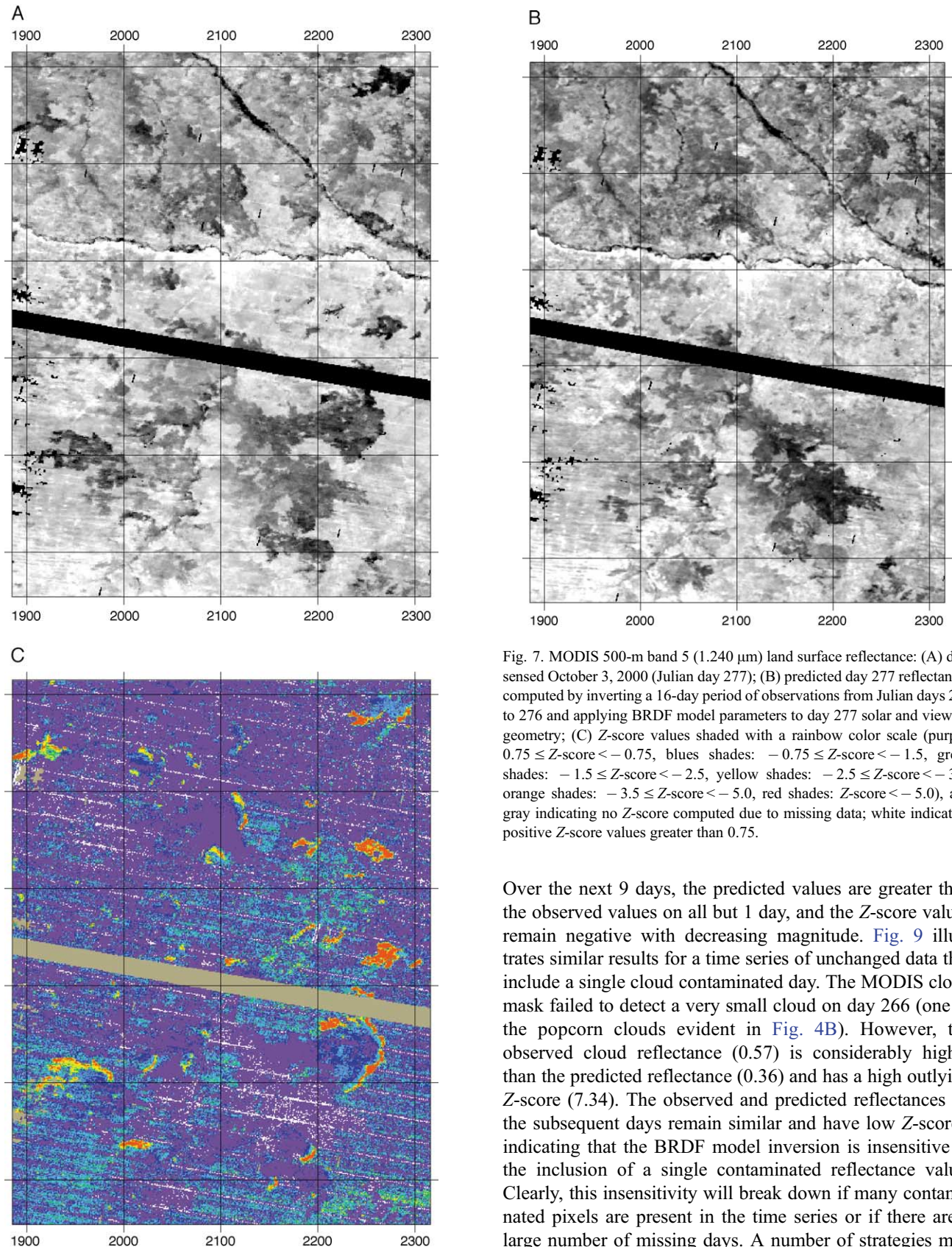
Fig. 7. MODIS 500-m band 5 (1.240 μm) land surface reflectance: (A) data sensed October 3, 2000 (Julian day 277); (B) predicted day 277 reflectances computed by inverting a 16-day period of observations from Julian days 261 to 276 and applying BRDF model parameters to day 277 solar and viewing geometry; (C) Z-score values shaded with a rainbow color scale (purple: $0.75 \leq Z$-score < -0.75, blues shades: $-0.75 \leq Z$-score < -1.5, green shades: $-1.5 \leq Z$-score < -2.5, yellow shades: $-2.5 \leq Z$-score < -3.5, orange shades: $-3.5 \leq Z$-score < -5.0, red shades: Z-score < -5.0), and gray indicating no Z-score computed due to missing data; white indicating positive Z-score values greater than 0.75.

Over the next 9 days, the predicted values are greater than the observed values on all but 1 day, and the Z-score values remain negative with decreasing magnitude. Fig. 9 illustrates similar results for a time series of unchanged data that include a single cloud contaminated day. The MODIS cloud mask failed to detect a very small cloud on day 266 (one of the popcorn clouds evident in Fig. 4B). However, the observed cloud reflectance (0.57) is considerably higher than the predicted reflectance (0.36) and has a high outlying Z-score (7.34). The observed and predicted reflectances on the subsequent days remain similar and have low Z-scores, indicating that the BRDF model inversion is insensitive to the inclusion of a single contaminated reflectance value. Clearly, this insensitivity will break down if many contaminated pixels are present in the time series or if there are a large number of missing days. A number of strategies may
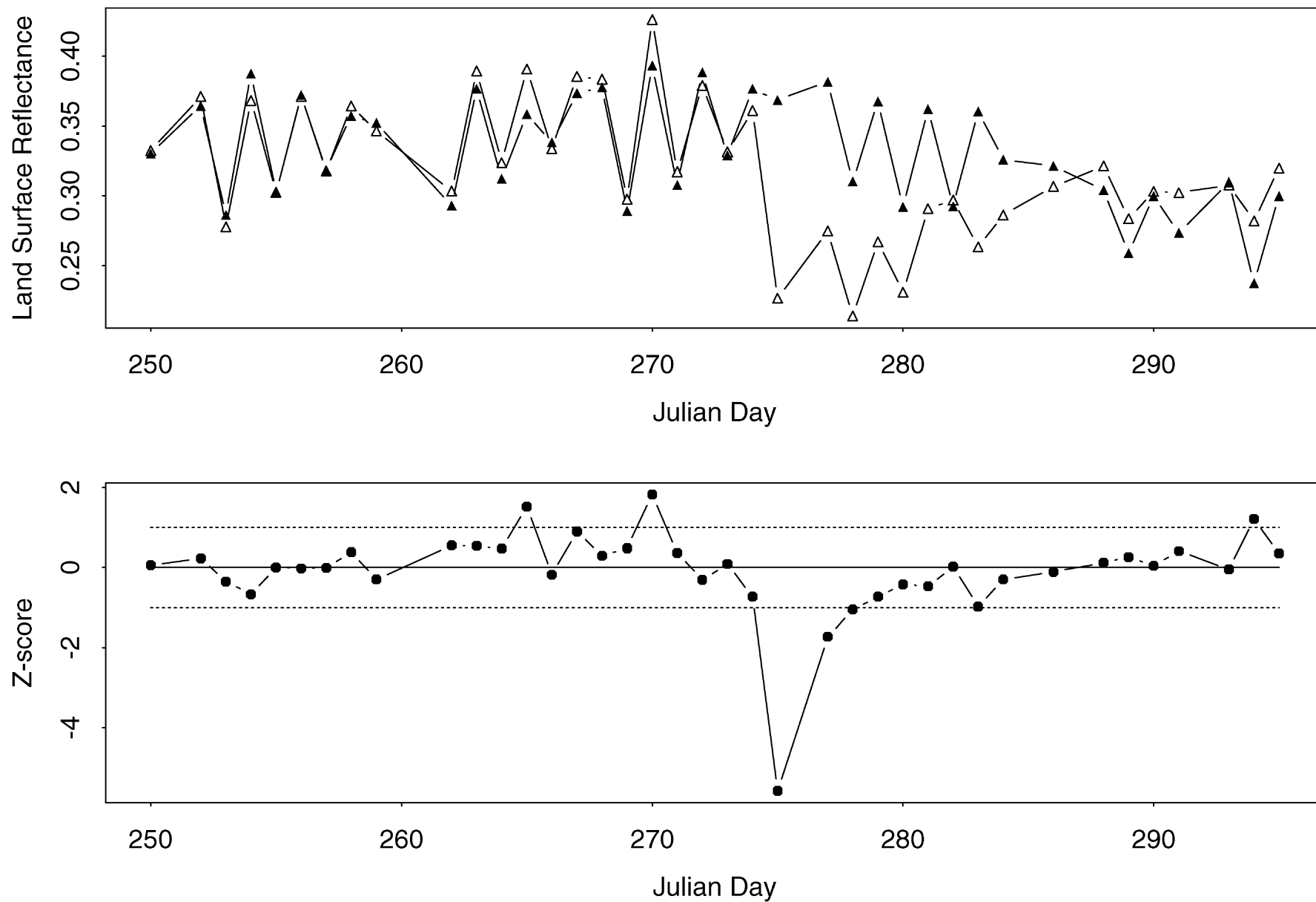
Fig. 8. Time series of observed (open triangles) and BRF predicted (filled triangles) MODIS 500-m band 5 (1.240 μm) land surface reflectance data and Z-score values (circles) for a single pixel located near the Angolan–Nambian border over a 46-day period (7 missing days). The lower panel dashed lines indicate Z-score values of ± unity. The pixel burned on day 275.
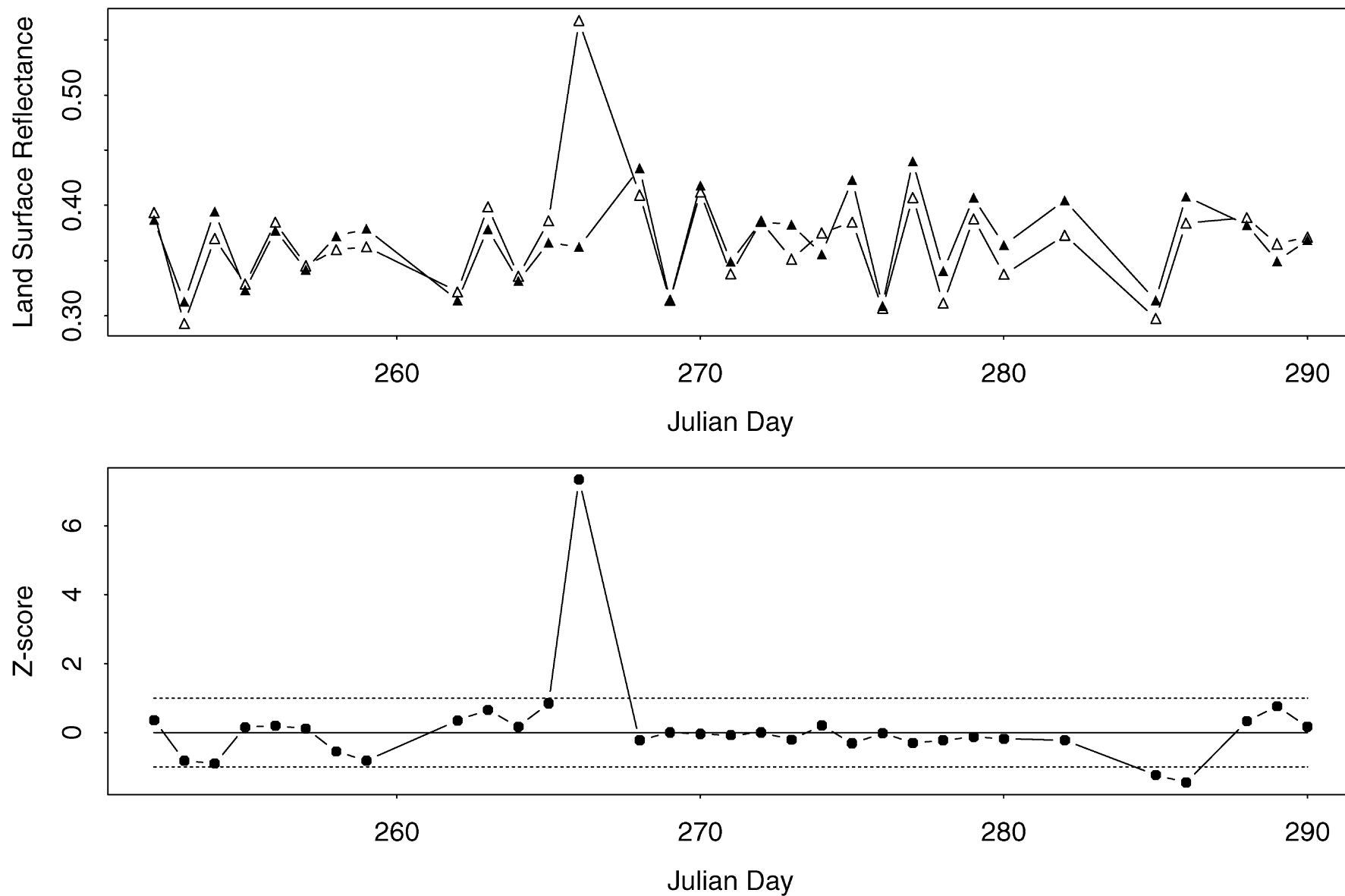
Fig. 9. Time series of observed (open triangles) and BRF predicted (filled triangles) MODIS 500-m band 5 (1.240 μm) land surface reflectance data and Z-score values (circles) for a single unburned pixel located near the Angolan–Nambian border over a 39-day period (6 missing days). The lower panel dashed lines indicate Z-score values of ± unity. The isolated high reflectance (0.57) value on day 266 corresponds to a
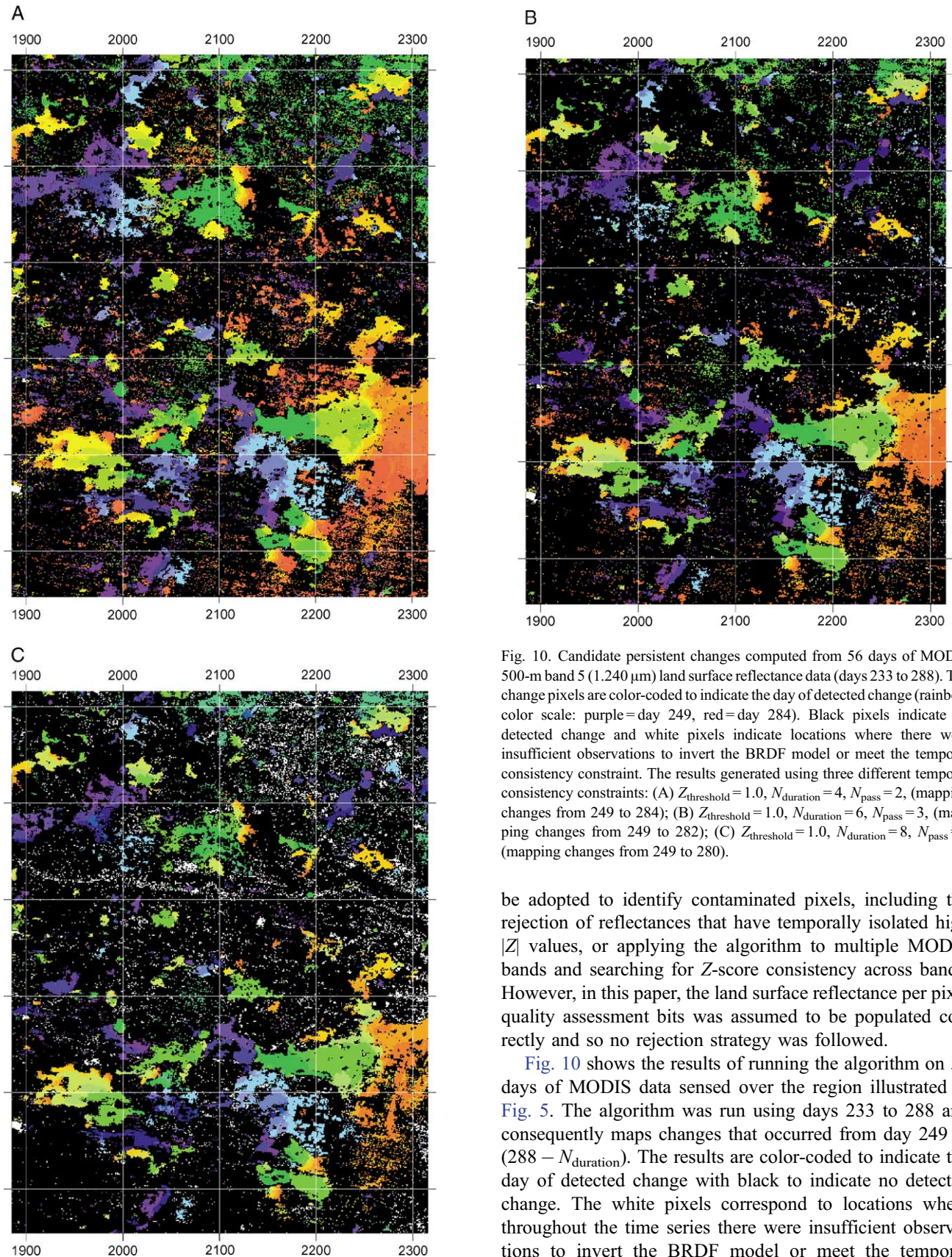
A

B

C

Fig. 10. Candidate persistent changes computed from 56 days of MODIS 500-m band 5 (1.240 μm) land surface reflectance data (days 233 to 288). The change pixels are color-coded to indicate the day of detected change (rainbow color scale: purple = day 249, red = day 284). Black pixels indicate no detected change and white pixels indicate locations where there were insufficient observations to invert the BRDF model or meet the temporal consistency constraint. The results generated using three different temporal consistency constraints: (A) $Z_{threshold} = 1.0$, $N_{duration} = 4$, $N_{pass} = 2$, (mapping changes from 249 to 284); (B) $Z_{threshold} = 1.0$, $N_{duration} = 6$, $N_{pass} = 3$, (mapping changes from 249 to 282); (C) $Z_{threshold} = 1.0$, $N_{duration} = 8$, $N_{pass} = 4$ (mapping changes from 249 to 280).

be adopted to identify contaminated pixels, including the rejection of reflectances that have temporally isolated high $|Z|$ values, or applying the algorithm to multiple MODIS bands and searching for Z-score consistency across bands. However, in this paper, the land surface reflectance per pixel quality assessment bits was assumed to be populated correctly and so no rejection strategy was followed.

Fig. 10 shows the results of running the algorithm on 56 days of MODIS data sensed over the region illustrated in Fig. 5. The algorithm was run using days 233 to 288 and consequently maps changes that occurred from day 249 to $(288 - N_{duration})$. The results are color-coded to indicate the day of detected change with black to indicate no detected change. The white pixels correspond to locations where throughout the time series there were insufficient observations to invert the BRDF model or meet the temporal
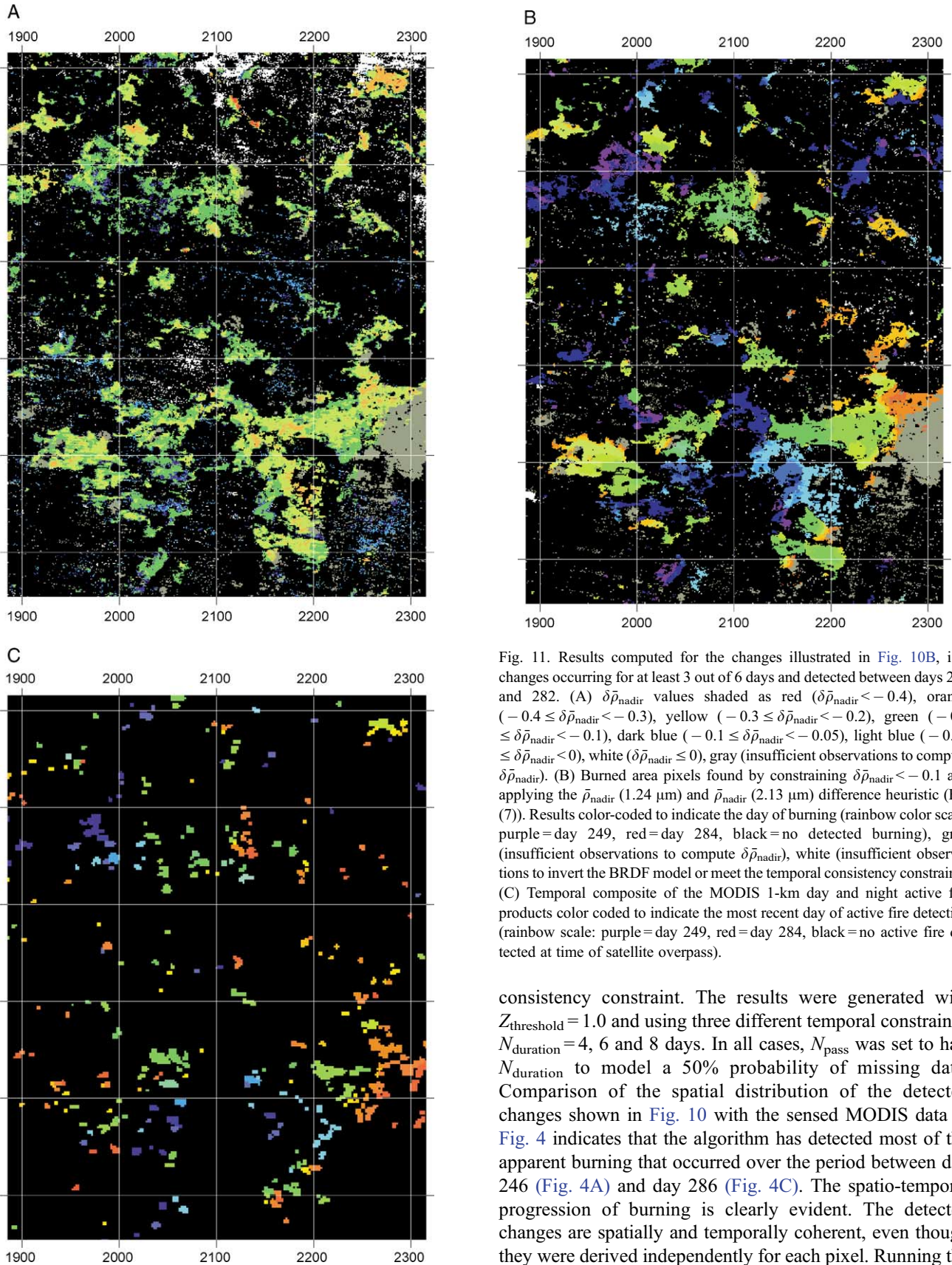
A

B

C

Fig. 11. Results computed for the changes illustrated in Fig. 10B, i.e., changes occurring for at least 3 out of 6 days and detected between days 249 and 282. (A) $\delta\bar{\rho}_{\mathrm{nadir}}$ values shaded as red ($\delta\bar{\rho}_{\mathrm{nadir}} < -0.4$), orange ($-0.4 \leq \delta\bar{\rho}_{\mathrm{nadir}} < -0.3$), yellow ($-0.3 \leq \delta\bar{\rho}_{\mathrm{nadir}} < -0.2$), green ($-0.2 \leq \delta\bar{\rho}_{\mathrm{nadir}} < -0.1$), dark blue ($-0.1 \leq \delta\bar{\rho}_{\mathrm{nadir}} < -0.05$), light blue ($-0.05 \leq \delta\bar{\rho}_{\mathrm{nadir}} < 0$), white ($\delta\bar{\rho}_{\mathrm{nadir}} \leq 0$), gray (insufficient observations to compute $\delta\bar{\rho}_{\mathrm{nadir}}$). (B) Burned area pixels found by constraining $\delta\bar{\rho}_{\mathrm{nadir}} < -0.1$ and applying the $\bar{\rho}_{\mathrm{nadir}}$ (1.24 μm) and $\bar{\rho}_{\mathrm{nadir}}$ (2.13 μm) difference heuristic (Eq. (7)). Results color-coded to indicate the day of burning (rainbow color scale: purple = day 249, red = day 284, black = no detected burning), gray (insufficient observations to compute $\delta\bar{\rho}_{\mathrm{nadir}}$), white (insufficient observations to invert the BRDF model or meet the temporal consistency constraint). (C) Temporal composite of the MODIS 1-km day and night active fire products color coded to indicate the most recent day of active fire detection (rainbow scale: purple = day 249, red = day 284, black = no active fire detected at time of satellite overpass).

consistency constraint. The results were generated with $Z_{\mathrm{threshold}} = 1.0$ and using three different temporal constraints, $N_{\mathrm{duration}} = 4$, 6 and 8 days. In all cases, N_{pass} was set to half N_{duration} to model a 50% probability of missing data. Comparison of the spatial distribution of the detected changes shown in Fig. 10 with the sensed MODIS data in Fig. 4 indicates that the algorithm has detected most of the apparent burning that occurred over the period between day 246 (Fig. 4A) and day 286 (Fig. 4C). The spatio-temporal progression of burning is clearly evident. The detected changes are spatially and temporally coherent, even though they were derived independently for each pixel. Running the
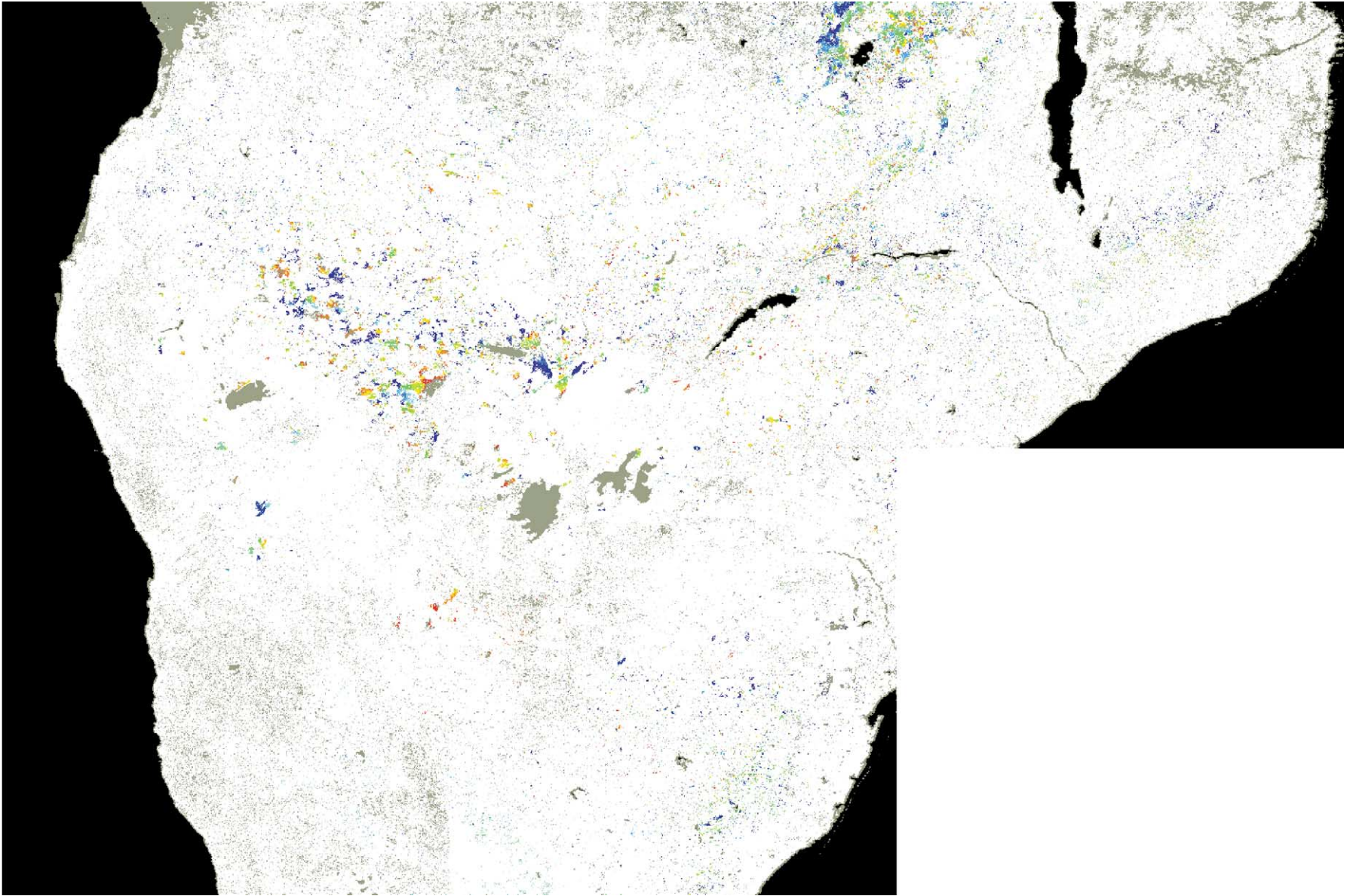
Fig. 12. Burned area map for study area (Fig. 1) showing the date and location of burning that occurred between Julian days 249 (September 5, 2000) and 282 (October 8, 2000). Burned areas shaded with a rainbow color scale to indicate the day of burning (purple = day 249, red = day 282), white (no burned areas detected), gray (insufficient observations to run the algorithm), black (water). Results generated from 56 days of data (Julian days 233–288, 2000) using $Z_{threshold} = 1.0$, $N_{duration} = 6$, $N_{pass} = 3$.

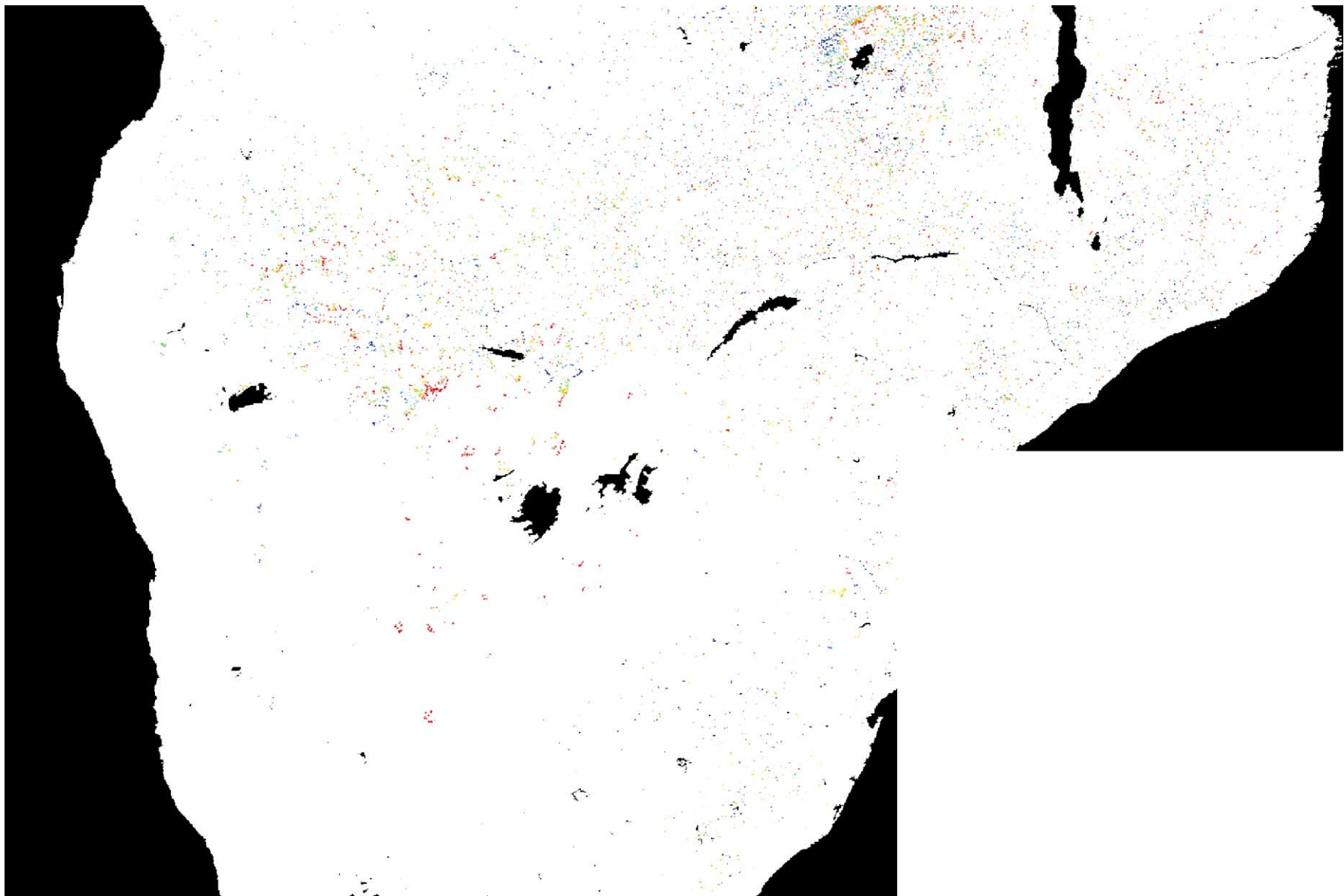Fig. 13. Temporal composite of the MODIS 1-km day and night active fire products for the study area (Fig. 1) for Julian days 249 (September 5, 2000) to 282 (October 8, 2000). Active fires shaded to indicate the most recent day of active fire detection (rainbow scale: purple = day 249, red = day 284), white (no active fire detected at time of satellite overpass), black (water and ephemeral water).

algorithm with increasing $N_{duration}$ for a fixed $Z_{threshold}$ reduces the number of detected changes. This is expected as in this region, burned areas have a progressively weaker "burn" signals as they age (Fig. 4) due to dissipation of charcoal and ash, and also, in this case limited, post-fire vegetation growth. Many of the burns are temporally persistent over at least an 8-day period (Fig. 10C). However, changes that are not associated with burning have also been detected. These changes are most apparent for smaller $N_{duration}$ and are generally spatially discontinuous. In certain cases, these changes are due to residual cloud and cloud shadow persistent in the data for several consecutive days.

Fig. 11A illustrates $\delta\bar{\rho}_{nadir}$ computed for the changes illustrated in Fig. 10B, i.e., changes detected between days 249 and 282. Positive $\delta\bar{\rho}_{nadir}$ values (shaded white) correspond to changes associated with an increase in $\bar{\rho}_{nadir}$ (1.24 μm) and are most likely associated with residual cloud contamination (Fig. 9). The gray shades in Fig. 11A indicate those pixels where there were insufficient observations to compute $\delta\bar{\rho}_{nadir}$. The remaining $\delta\bar{\rho}_{nadir}$ values are negative and are color-coded to show their magnitude. The greatest $\delta\bar{\rho}_{nadir}$ values (< -0.3) primarily occur towards the interior of the burned areas. The edges of these areas and the less spatially continuous detected changes have $\delta\bar{\rho}_{nadir}$ from 0.0 to -0.2. Fig. 11B shows the result of thresholding $\delta\bar{\rho}_{nadir}$ to discard change candidates where $\bar{\rho}_{nadir}$ (1.24 μm) decreased by less than 0.1 and applying the $\bar{\rho}_{nadir}$ (1.24 μm) and $\bar{\rho}_{nadir}$ (2.13 μm) difference heuristic (Eq. (7)). The resulting changes are assumed to be due to burning. The burned areas are color-coded to indicate the day of detected burning with black to indicate no detected change. For comparative purposes, Fig. 11C shows a temporal composite of the MODIS 1-km day and night active fire products for the corresponding detection period (days 249–282). The temporal progression of the active fires detected by MODIS over this period is clearly evident. Generally, a strong correspondence is observed between the *locations* and *dates* of the 500-m burn results and the 1-km active fires. The majority of the detected active fire pixels and the regions between them are labeled as burned. Several of the later (day 282) active fires are shaded gray in the burned area result (Fig. 11B) because insufficient observations were available at the end of the time series to compute $\delta\bar{\rho}_{nadir}$. However, examination of these locations in Fig. 10b indicates that they were detected. Fig. 12 illustrates the application of the algorithm to the Southern Africa study region mapping the burned areas that occurred between Julian days 249 and 282 (September 5 to October 8, 2000). The results are color-coded to indicate the day of burning (white indicates no burning detected and gray indicates locations where there were insufficient observations to invert the BRDF model or to meet the temporal consistency constraint or to compute $\delta\bar{\rho}_{nadir}$). The Etosha and Makgadikgadi pans and some other regions were consistently flagged as cloudy or ephemeral water and so were not considered by the algorithm. Fig. 13 shows a temporal composite of the MODIS 1-km day and

night active fire products for the corresponding period. A very high degree of biomass burning is evident across the region. Even at this small scale, it is apparent that the timing and location of the larger burned areas correspond to the active fire detection results. Qualitatively, the distribution of burning is broadly similar to results found in previous years using coarse spatial resolution 5-km AVHRR data (Barbosa, Stroppiana, Gregoire, & Pereira, 1999). At the time of writing, validation of these data is in progress and further refinements are envisioned, pending the availability of independent validation data.

7. Conclusion and discussion

The BRDF model-based expectation change detection algorithm developed in this paper appears to be effective in detecting burned areas across Southern Africa. Preliminary regional verification, provided by comparison of the MODIS active fire product with the algorithm results generated from approximately 2 months of MODIS data, indicate that the algorithm maps both the location and approximate day of burning. Separability analysis of the MODIS land surface reflectance bands indicates that for the Southern Africa study area land surface reflectance in MODIS band 5 (1.240 μm) provides the best burned–unburned discrimination followed by band 2 (0.858 μm) and band 6 (1.640 μm).

The results presented in this paper were generated from MODIS 500-m band 5 (1.240 μm) land surface reflectance with an additional heuristic that used 500-m band 7 (2.130 μm) reflectance to discard changes not associated with burning. Applying the algorithm independently to MODIS 500-m band 6 and band 2 land surface reflectance data provided similar results, though they are not described in this paper. The combined use of these bands may provide more reliable results. Further research will be undertaken to investigate if the algorithm can be applied reliably to a time series of 250-m MODIS band 2 (0.858 μm) land surface reflectance and to investigate to what extent regional burned area estimates are improved using 250-m rather than 500-m data. The high spatial and temporal resolution of the MODIS burned area data may meet requirements for local and regional uses of burned area data sets (e.g., for resource management and environmental assessment) in addition to regional and global uses (e.g., for study of atmospheric processes and greenhouse gas inventories). Collaborative research is being initiated to assess the utility of MODIS burned area data in the context of these two scales of study.

The described BRDF model-based expectation change detection algorithm is an improvement on previous change detection methods due to two main factors, namely the use of a BRDF model to deal with angular variations observed in multi-temporal satellite data, and the use of a statistical measure to detect change from a previously observed state.

The former of these effectively improves the signal-to-noise ratio of the data, and the latter somewhat objectifies the selection of threshold(s) used to determine change of state. The method is adaptive to the number, viewing and illumination geometry of the data, and to the amount of noise in the data. The method labels change pixels as those where change is detected in a consistent manner for a specified number of days. Residual cloud, shadow, and other undesirable data are removed through use of this temporal consistency constraint. The approach can be considered a generic change detection method and provides a route for the use of multiple data sources and observations of varying degrees of uncertainty within a rigorous modeling framework.

Application of the algorithm to the specific problem of detecting burned areas has necessitated the incorporation of several heuristics that require further examination, pending the availability of independent validation data. Further related research includes consideration of the following: (i) how the algorithm operates on multiple wavebands; (ii) how the algorithm handles sub-pixel variations in the proportion of the pixels that are burned; (iii) how spatial contextual information might be used (e.g., increasing expectation of a burn in pixels neighboring detected burned areas or active fires); (iv) how changes due to burning can be differentiated from other types of sudden change (e.g., leaf flushing caused by a sudden rainfall event); (v) how the temporal consistency thresholds ($N_{duration}$ and N_{pass}) can be determined reliably; and (vi) how the algorithm performs in regions with different fire regimes (e.g., different arrangements of different land covers with different surface bidirectional reflectance properties and burn persistence). There are several issues underlying the generic change approach that also merit further attention, namely: (i) consideration of the temporal dynamics of the vegetation; and (ii) the assumption of equal weighting for all observations. These are described briefly below.

The algorithm presented here is based on the assumption that the surface state remains static over the n days of the moving window. As long as this period is kept short, this may be a reasonable assumption, but persistent cloud effects may necessitate a compromise between this criterion and the requirement for a sufficient number of observations, m, required for modeling. For the MODIS application, we used $n = 16$ and $m = 7$. If a longer temporal window is considered, a model of the expected temporal evolution of the model parameters may be required. This concept is attractive in that it would allow for a more reliable prediction of change in cases where there are large numbers of missing observations, and could allow for an increase in uncertainty in predicted reflectance as the time from the last observation increased. One framework for the integration of such a temporal model with the existing approach is Kalman filtering (Maybeck, 1979). Unfortunately, we do not yet have sufficient data on the temporal dynamics of BRDF model parameters to attempt a reliable modeling of this sort.

For MODIS application, the combined utility of Terra and Aqua MODIS data sensed with morning and afternoon overpass times (Kaufman et al., 1998) may increase the number of cloud-free observations and reduce the requirement for this algorithm refinement. Combining MODIS data with "similar" observations from other sensors such as MISR, SPOT VEGETATION, or the forthcoming MSG-SEVIRI and MERIS instruments, might improve our ability to detect burned areas by providing additional observations. This will, however, require precise co-registration and combining information from different wavebands, a concept that would need to be integrated into the modeling framework.

The assumption of equal weighting of all observations in the BRDF model inversion is strictly valid only if the variance expected for each observation is equal. There are several reasons why this is not typically the case: (i) the projected instantaneous field-of-view of an instrument such as MODIS increases with increasing view zenith angle (Wolfe et al., 1998); (ii) the variance at a location is intrinsically a function of viewing and illumination conditions, even if the projected instantaneous field-of-view is kept constant (Ni & Jupp, 2000). The "spatial smoothing" effect of the former is to reduce the pixel variance for off-nadir observations (Ni & Jupp, 2000). The effects of the latter are more complicated and vary as a function of surface state and wavelength (Lewis, Disney, & Riedmann, 1999). If we can effectively model both of these effects, or derive such information from the data themselves, it would be straightforward to incorporate expected observation variance into the method of least squares or any Kalman filtering approach. The challenge for further research is to provide this information.

At the time of writing, rigorous validation of the MODIS burned area results has not been performed. Collection of independent validation data sets has been undertaken as part of the Southern African Regional Science Initiative (SAFARI 2000) dry season field campaign (Swap et al., 2002) by members of the Southern African Fire Network), which is emerging from the Miombo Network (Desanker, Frost, Justice, & Scholes, 1997), and GOFC-Fire initiatives (GOFC Design Team, 1999). Collaborating members in Namibia, Zambia, Botswana, South Africa, Zimbabwe, and Mozambique were provided in 2000 with a total of 28 Landsat ETM scenes acquired on two or more dates at sites that encompass a range of environmental, land use, and fire management conditions. They used the Landsat ETM data to make burned area maps following a consensus protocol. These higher spatial resolution Landsat ETM burned area data sets will be compared with the MODIS regional burned area data to quantify and explain errors of omission and commission and to investigate the future research topics described above. The research presented in this paper provides a new approach to burned area mapping and the basis for algorithm development of the MODIS burned area product.

Acknowledgements

References

Ackerman, S. A., Strabala, K. I., Menzel, W. P., Frey, R. A., Moeller, C. C., & Gumley, L. E. (1998). Discriminating clear sky from clouds with MODIS. *Journal of Geophysical Research*, *103*, 32141–32157.

Arino, O., & Rosaz, J. (1999). 1997 and 1998 world ATSR Fire atlas using ERS-2 ATSR-2 data. *Proceedings of the joint fire science conference, Boise, 15–17 June, Volume 1* (pp. 177–182). University Idaho, Idaho, USA.

Barbosa, P. M., Gregoire, J.-M., & Pereira, J. M. C. (1999). An algorithm for extracting burned areas from time series of AVHRR GAC data applied at a continental scale. *Remote Sensing of Environment*, *69*, 253–263.

Barbosa, P. M., Stroppiana, D., Gregoire, J.-M., & Pereira, J. M. C. (1999). An assessment of vegetation fire in Africa (1981–1991): burned areas, burned biomass and atmospheric emissions. *Global Biogeochemcial Cycles*, *13*, 933–950.

Barnes, W. L., Pagano, T. S., & Salomonson, V. V. (1998). Prelaunch characteristics of the moderate resolution imaging spectroradiometer (MODIS) on EOS-AM1. *IEEE Transactions on Geoscience and Remote Sensing*, *36*, 1088–1100.

Barnsley, M. J., Allison, D., & Lewis, P. (1997). On the information content of multiple-view-angle (MVA) data sets. *International Journal of Remote Sensing*, *18*, 1937–1960.

Bird, M. I., & Cali, J. A. (1998). A million-year record of fire in sub-Saharan Africa. *Nature*, *394*(6695), 767–769.

Braatz, B. V., Brown, S., Isichei, A. O., Odada, E. O., Scholes, R. J., Sokona, Y., Drichi, P., Gaston, G., Delmas, R., Holmes, R., Amous, S., Muyungi, R. S., DeJode, A., & Gibbs, M. (1995). African greenhouse gas emission inventories and mitigation options: forestry, land-use change, and agriculture. *Environmental Monitoring and Assessment*, *38*, 109–126.

Cahoon, D. R., Stocks, B. J., Levine, J. S., Cofer, W. R., & Pierson, J. M. (1994). Satellite analysis of the severe 1987 forest-fires in northern China and southeastern Siberia. *Journal of Geophysical Research-Atmospheres*, *99*(D9), 18627–18638.

Crutzen, P. J., & Andreae, M. O. (1990). Biomass burning in the tropics: impact on atmospheric chemistry and biogeochemical cycles. *Science*, *250*, 1669–1678.

Desanker, P. V., Frost, P. G. H., Justice, C. O., Scholes, R. J. (1997). *The Miombo network: framework for a terrestrial transect study of land-use and land-cover change in the Miombo ecosystems of central Africa.* IGBP Report 41, International Geosphere-Biosphere Programme, Stockholm, Sweden.

Dwyer, E., Pinnock, S., Gregoire, J. M., & Pereira, J. M. C. (2000). Global spatial and temporal distribution of vegetation fire as determined from satellite observations. *International Journal of Remote Sensing*, *21*, 1289–1302.

Eva, H., & Lambin, E. F. (1998a). Burnt area mapping in Central Africa using ATSR data. *International Journal of Remote Sensing*, *19*, 3473–3497.

Eva, H., & Lambin, E. F. (1998b). Remote sensing of biomass burning in tropical regions: sampling issues and multisensor approach. *Remote Sensing of Environment*, *64*, 292–315.

Fernandez, A., Illera, P., & Casanova, J. L. (1997). Automating mapping of surfaces affected by forest fires in Spain using AVHRR NDVI composite image data. *Remote Sensing of Environment*, *60*, 153–162.

Fraser, R. H., Li, Z., & Cihlar, J. (2000). Hotspot and NDVI differencing synergy (HANDS): a new technique for burned area mapping over boreal forest. *Remote Sensing of Environment*, *74*, 362–376.

Fredericksen, P. S., Langaas, S., & Mbaye, M. (1990). NOAA-AVHRR and GIS-based monitoring of fire activity in Senegal—a provisional methodology and potential applications. In J. G. Goldammer (Ed.), *Fire in the tropical biota: ecosystem processes and global challenges. Ecological Studies, vol. 84* (pp. 400–417). Berlin: Springer-Verlag.

Frost, P. G. H. (1999). Fire in southern African woodlands: origins, impacts, effects, and control. Proceedings of an FAO meeting on public policies affecting forest fires. *FAO Forestry Paper*, *138*, 181–205.

Fukunaga, K. (1990). *Introduction to statistical pattern recognition* (2nd ed.) (p. 188). Boston, USA: Academic Press.

Garstang, M., Tyson, P. D., Swap, R., Edwards, M., Kållberg, P., & Lindesay, J. A. (1996). Horizontal and vertical transport of air over southern Africa. *Journal of Geophysical Research*, *101*(D19), 23713–23720.

Giglio, L., Kendall, J. D., & Justice, C. O. (1999). Evaluation of global fire detection algorithms using simulated AVHRR infrared data. *International Journal of Remote Sensing*, *20*, 1947–1985.

Goel, N. S., & Thompson, R. L. (2000). A snapshot of canopy reflectance models and a universal model for the radiation regime. *Remote Sensing Reviews*, *18*, 197–225.

GOFC Design Team. (1999). *A strategy for global observation of forest cover*, Version 1.2, January 4, 1999.

Hao, W. M., Lui, M.-H., & Crutzen, P. J. (1990). Estimates of annual and regional releases of CO2 and other trace gases to the atmosphere from fires in the tropics, based on FAO statistics for the period 1975–1980. In J. G. Goldammer (Ed.), *Fire in the tropical biota: ecosystem processes and global challenges. Ecological Studies, vol. 84* (pp. 440–462). Berlin: Springer-Verlag.

Justice, C. O. (1999). Introduction of *The Report of the 4th IGBP-DIS Fire Working Group Meeting, IGBP-DIS Working Paper #21*, Toulouse, France, 19–20 March 1998, IGBP-DIS Office, CNRM, 42, Avenue Gustave Coriolis, 31057 Toulouse Cedex, France.

Justice, C. O., Giglio, L., Korontzi, S., Owens, J., Alleaume, S., Morisette, J. T., Roy, D. P., Petitecolin, F., Descloitres, J., & Kaufman, Y. (2002). Global fire products from MODIS. (Special Issue of) *Remote Sensing of Environment, 83*, 245–263 (this issue).

Kasischke, E. S., & French, N. H. F. (1995). Locating and estimating the areal extent of wildfires in Alaskan boreal forests using multiple-season AVHRR NDVI composite data. *Remote Sensing of Environment*, *51*, 263–275.

Kaufman, Y. J., Justice, C. O., Flynn, L. P., Kendall, J. D., Prins, E. M., Giglio, L., Ward, D. E., Menzel, W. P., & Setzer, A. W. (1998). Potential global fire monitoring from EOS-MODIS. *Journal of Geophysical Research-Atmospheres*, *103*, 32215–32238.

Kaufman, Y. J., & Remer, L. (1994). Detection of forests using mid-IR reflectance: an application for aerosol studies. *IEEE Transactions on Geoscience and Remote Sensing*, *32*, 672–683.

Langaas, S. (1995). *Night-time observations of West-African bushfires from space: studies on methods and applications of thermal NOAA/AVHRR satellite data from Senegal and the Gambia*. PhD thesis, Department of Geography, University of Oslo, Norway.

Leroy, M., & Hautecoeur, O. (1999). Anisotropy-corrected vegetation indexes derived from POLDER ADEOS. *IEEE Transactions on Geoscience and Remote Sensing*, *37*, 1698–1708.

Levine, J. S. (Ed.) (1996). *Biomass burning and global change*. Cambridge, MA: MIT Press.

Lewis, P. E., Disney, M. I., & Riedmann, M. (1999). Application of the botanical plant modelling system (BPMS) to the analysis of spatial information in remotely sensed imagery. *Proc. 25th annual remote sensing society conference, 7–10th September, Cardiff, UK* (pp. 507–514).

Lucht, W., & Lewis, P. E. (2000). Theoretical noise sensitivity of BRDF and albedo retrieval from the EOS-MODIS and MISR sensors with respect to angular sampling. *International Journal of Remote Sensing*, *21*, 81–98.

Lucht, W., & Roujean, J.-L. (2000). Considerations in the parametric modeling of BRDF and Albedo from multiangular satellite sensor observations. *Remote Sensing Reviews*, *18*, 343–379.

Maybeck, P. S. (1979). *Stochastic models, estimation and control, volume 1*. New York: Academic Press.

McDonald, A. J., Gemmell, F. M., & Lewis, P. E. (1998). Investigation of the utility of spectral vegetation indices for determining information on coniferous forests. *Remote Sensing of Environment*, 66, 250–272.

Miura, T., Huete, A. R., van Leeuwen, W.J.D, & Didan, K. (1998). Vegetation detection through smoke filled AVIRIS images: an assessment using MODIS band passes. *Journal of Geophysical Research*, 103 (D24), 32001–32011.

Ni, W., & Jupp, D. L. B. (2000). Spatial variance in directional remote sensing imagery—recent developments and future perspectives. *Remote Sensing Reviews*, 18, 441–479.

Nolin, A. W., & Liang, S. (2000). Progress in bi-directional reflectance modeling and applications for surface particulate media: snow and soils. *Remote Sensing Reviews*, 18, 307–342.

Pereira, J. M. C., Chuvieco, E., Beaudoin, A., & Desbois, N. (1997). Remote sensing of burned areas: a review. *A review of remote sensing methods for the study of large wildland fires.* In E. Chuvieco (Ed.), (1997). *Report of the Megafires Project ENV-CT96-0256, August 1997*, (pp. 127–183). Alcala de Henares, Spain: Universidad de Alcala.

Petitcolin, F., & Vermote, E. F. (2002). Land surface reflectance, emissitivity and temperature from MODIS middle and thermal infrared data. (Special Issue of) *Remote Sensing of Environment, 83*, 112–134.

Roujean, J.-L., Leroy, M., & Deschamps, P. Y. (1992). A bi-directional reflectance model of the Earth's surface for the correction of remote sensing data. *Journal of Geophysical Research*, 97, 20255–20468.

Roy, D. P. (2000). The impact of misregistration upon composited wide field of view satellite data and implications for change detection. *IEEE Transactions on Geoscience and Remote Sensing*, 38, 2017–2032.

Roy, D. P., Borak, J. S., Devadiga, S., Wolfe, R. E., Zheng, M., & Descloitres, J. (2002). The MODIS land product quality assessment approach. (Special Issue of) *Remote Sensing of Environment, 83*, 62–76.

Roy, D. P., Giglio, L., Kendall, J. D., & Justice, C. O. (1999). Multitemporal active-fire based burn scar detection algorithm. *International Journal of Remote Sensing*, 20, 1031–1038.

Roy, D. P., & Lewis, P. E. (2000). Burned area mapping from multitemporal surface bi-directional reflectance. (Presented at) American Geophysical Union Spring 2000 Meeting, Session B04: Remote Sensing of the Biosphere, Washington, DC, May 30–June 3, 2000.

Schaaf, C. B., Gao, F., Strahler, A. H., Lucht, W., Li, X., Tsang, T., Strugnell, N., Zhang, X., Jin, Y., Muller, J.-P., Lewis, P. E., Barnsley, M., Hobson, P., Disney, M., Roberts, G., Dunderdale, M., Doll, C., d'Entremont, R. P., Hu, B., Liang, S., Privette, J., & Roy, D. P. (2002). First operational BRDF, Albedo and Nadir reflectance products from MODIS. (Special Issue of) *Remote Sensing of Environment, 83*, 135–148.

Scholes, R. J., Ward, D. E., & Justice, C. O. (1996). Emissions of trace gases and aerosol particles due to vegetation burning in southern hemisphere Africa. *Journal of Geophysical Research*, 101(D19), 23677–23682.

Stocks, B. J., Goldammer, J. G., Cahoon, D. R., & Frost, P. (1999). Global fire monitoring: international policy requirements. *Forest fire monitoring and mapping: a component of global observation of forest cover, November 3–5 1999* (pp. 79–84). Ispra, Italy: JRC.

Stroppiana, D., Pinnock, S., & Gregoire, J.-M. (2000). The global fire product: daily occurrence from April 1992 to December 1993 derived from NOAA AVHRR data. *International Journal of Remote Sensing*, 21, 1279–1288.

Swap, R. J., Annegarn, H. J., Suttles, J. T., Haywood, J., Helmlinger, M. C., Hely, C., Hobbs, P. V., Holben, B. N., Ji, J., King, M., Landmann, T., Maenhaut, W., Otter, L., Pak, B., Piketh, S. J., Platnick, S., Privette, J., Roy, D. P., Thompson, A. M., Ward, D., & Yokelson, R. (2002). The Southern African Regional Science Initiative (SAFARI 2000): overview of the dry-season field campaign. *South African Journal of Science*, 98, 125–130.

Trigg, S., & Flasse, S. (2000). Characterizing the spectral–temporal response of burned Savannah using in situ spectroradiometry and infrared thermometry. *International Journal of Remote Sensing*, 21, 3161–3168.

Vermote, E. F., El Saleous, N. Z., & Justice, C. O. (2002). Atmospheric correction of MODIS data in the visible to middle infrared: first results. (Special Issue of) *Remote Sensing of Environment, 83*, 97–111.

Wan, Z., Zhang, Y., Zhang, Q., & Li, Z.-L. (2002). Validation of the land-surface temperature products retrieved from Terra moderate resolution imaging spectroradiometer data. (Special Issue of) *Remote Sensing of Environment, 83*, 163–180.

Wanner, W., Li, X., & Strahler, A. H. (1995). On the derivation of kernels for kernel-driven models of bi-directional reflectance. *Journal of Geophysical Research*, 100, 21077–21090.

Wanner, W., Strahler, A. H., Hu, B., Lewis, P., Muller, J.-P., Li, X., Schaaf, C., & Barnsley, M. J. (1997). Global retrieval of bi-directional reflectance and albedo over land from EOS MODIS and MISR Data: theory and algorithms. *Journal of Geophysical Research*, 102, 17143–17162.

Whittaker, E., & Robinson, G. (1960). *The calculus of observations* (4th ed.). Glasgow: Blackie & Son.

Wolfe, R. E., Nishihama, M., Fleig, A., Kuyper, J., Roy, D. P., Storey, J., & Patt, F. (2002). Achieving sub-pixel geolocation accuracy in support of MODIS land science. (Special Issue of) *Remote Sensing of Environment, 83*, 31–49.

Wolfe, R. E., Roy, D. P., & Vermote, E. F. (1998). The MODIS land data storage, gridding and compositing methodology: L2 grid. *IEEE Transactions on Geoscience and Remote Sensing*, 36, 1324–1338.

Zhan, X., Sohlberg, R., Townshend, J. R. G., DiMiceli, C., Carroll, M., Eastman, J. C., Hansen, M., & DeFries, R. S. (2002). Detection of land cover changes using MODIS 250 m data. (Special Issue of) *Remote Sensing of Environment, 83*, 337–351.